Clot Machining in the Brain Vessels

by

Yang Liu

A dissertation submitted in partial fulfillment
of the requirements for the degree of
Doctor of Philosophy
(Mechanical Engineering)
in the University of Michigan
2019

Doctoral Committee:

Professor Albert J. Shih, Chair
Lecturer Barry Belmont
Associate Professor Eric Johnsen
Professor Brian J. Love
Dr. Luis E. Savastano
Dr. Yihao Zheng

Yang Liu

yliume@umich.edu

ORCID iD: 0000-0002-9132-0258

DEDICATION

To my wonderful parents.

ACKNOWLEDGMENTS

I truly appreciate everyone that has helped me along my way through this doctorate degree. I regret not being able to put everyone's name down here, but I will try my best to name a few.

First, I would like to express my greatest appreciation to my advisor, Prof. Albert Shih. He gave me the opportunity to start this journey and has provided unconditional support ever since. He helped me with not only research, but also presentation skills, networking, and overall career development. For me, he is a model of hardworking researcher, influential advisor, enthusiastic teacher, and warm father.

I also want to express my great gratitude to my dissertation committee for their guidance and suggestions. Besides that, I'd like to thank Prof. Brian Love for actively looking for collaboration and funding opportunity for my research. I'd like to thank Prof. Eric Johnsen for always being encouraging and passing me the philosophy of conducting numerical modelling. I'd like to thank Dr. Barry Belmont for inspiring me with his critical thinking and passion in research since the early days of my journey. I would like to thank Dr. Yihao Zheng for being my mentor in many aspects beside academics since I started this journey. I'd like to thank Dr. Luis Savastano, the most talented and yet hardworking doctor I have ever seen. His enthusiasm in conducting impactful research have motivated me all the time. Without his support, I can't achieve what I have achieved today.

I would like to thank all my current and past lab mates at the Biomedical Manufacturing and Design Lab in the S. M. Wu Manufacturing Research Center for making me feel like being in a warm family, including (in no particular order): Ketut Bagus Priambada, Dian-Ru (Annie) Li, Robert Chisena, Jeff Plott, Lei Chen, Matthew Hildner, Jingxuan (Jessie) Lyu, Tianshu (Kelly) Dong, Zhaoju Zhu, Yuanqiang Luo, Dan Zhou, Roland Chen, and Bruce Tai. Special

thanks to the research assistants who works with me closely day in day out to develop this technology: Joshua Cockrum, Adithya Reddy, Daniel Gebrezgiabhier, and Evan Davis.

I'd like to thank the NeuroIR team at the University of Michigan Health System for their assistance in obtaining clots and catheters from mechanical thrombectomy procedures and feedback on my research. Thanks to the University of Michigan Blood Bank for the continuous support of providing blood products.

Additional thanks to the funding agencies that supports this project: the UM Coulter Translational Research Partnership Program (Thomas Marten and Matthew Okoneski), the National Institute of Health Centers for Accelerated Innovations of the NHLBI, and the Michigan Translational Research and Commercialization Innovation Hub. I also want to thank the National Science Foundation (NSF) and the Lightweight Innovations for Tomorrow (LIFT) for the support of my side projects.

Last but not least, I want to say thank you to my parents, sister, and girlfriend for making this journey full of fun.

TABLE OF CONTENTS

LIST OF TABLES

LIST OF FIGURES

ABSTRACT

Blood clots are clumps of coagulated blood and can adversely form, travel, and occlude a vessel in the brain, heart, lung, and extremities, causing stroke, myocardial infarction, pulmonary embolism, and deep vein thrombosis, respectively. Stroke is the fifth cause of death and leading cause of long-term disability in the US. To treat stroke, timely, completely, and minimally invasive removal of the clots to restore the blood flow is key. Mechanical thrombectomy is a catheter-based interventional procedural to remove clots and has become a standard of care for stroke since 2015.

Two types of mechanical thrombectomy devices have been approved. One is the suction catheter which vacuums the clots out. Another is the stent retriever which uses an expanded wire mesh to grasp and pull the clots out. These two devices are also used in combination. The success rate to achieve complete reperfusion of the previously occluded vascular territories is around 50%. Achieving complete clot removal is currently a major challenge.

This dissertation studies the clot removal mechanism of a cutting-based catheter. First, mechanical properties of 16 clots from stroke patients were analyzed by tensile test and their compositions were analyzed by histology. Second, 10 types of clot analogs (CAs) from human blood materials (red blood cells, plasma, and platelets) were fabricated to mimic the tensile and histological properties of the patient clots. Third, a cutting-based catheter was built with a miniature cutting tool and a smoothed particle Galerkin (SPG) model was developed to estimate the cutting forces. The SPG model was validated experimentally. Last, the fluid behavior near the catheter tip was observed by a high-speed camera and modelled by computational fluid dynamics.

Clots from patients were histologically and mechanically highly variant among and within patients. Clot compositions ranged from 0.45% to 91% (43%±35%) red blood cells, 0 to

95% (40%±37%) fibrin, and 1.7% to 56% (18%±16%) platelets. Clot tensile properties range from 105% to 489% (241%±104%) ultimate strain and 63 to 2396 kPa (569±695 kPa) ultimate stress. The ultimate strain was strongly ($|r| \geqslant 0.6$) and positively correlated with the platelet percentage and the ultimate tensile stress was strongly and positively correlated with the fibrin percentage. Similar correlations were also found in the CAs, which had an ultimate strain ranging from 0.78 to 1.36 and ultimate stress ranging from 16 to 949 kPa. A multi-variable regression model was built to guide the fabrication of CAs with desired histological compositions. For the difficult-to-remove clots, the cutting forces at rotational speeds of 60,000, 90,000, and 120,000 rpm were measured to be 0.74, 0.59, and 0.36 N, respectively and the predicted cutting forces from the SPG model matched the experiment measurements with errors less than 20%. During clot cutting, air bubbles could flow into the catheter due to air leakage. Clot chips could be pushed out of the catheter tip at about 2 m/s speed due to the vortex flow near the catheter tip and poor chip evacuation. To address those risks, a better seal is needed and the cavitation-assisted chip breaking can be introduced by the vortex-induced low pressure (< -99 kPa) zones.

These findings lay the groundwork for developing effective and safe mechanical thrombectomy devices. The clot tensile properties, as well as the experiment and modelling methodologies, can be applied to mechanical thrombectomy device development for a better stroke treatment.

CHAPTER 1
INTRODUCTION

1.1 Motivation

Blood clots are clumps of coagulated blood. Clots are usually formed, when a blood vessel is damaged, to prevent bleeding. The damaged vessel activates platelets in the blood and causes platelet aggregation and adhesion to the damaged site, forming a "plug" [1]. The damaged vessel and activated platelets also trigger a series of enzymatic reactions that form enzyme thrombin to convert fibrinogen in the plasma to a fibrin network [2], trapping platelets and red blood cells (RBC), as shown in Figure 1.1.

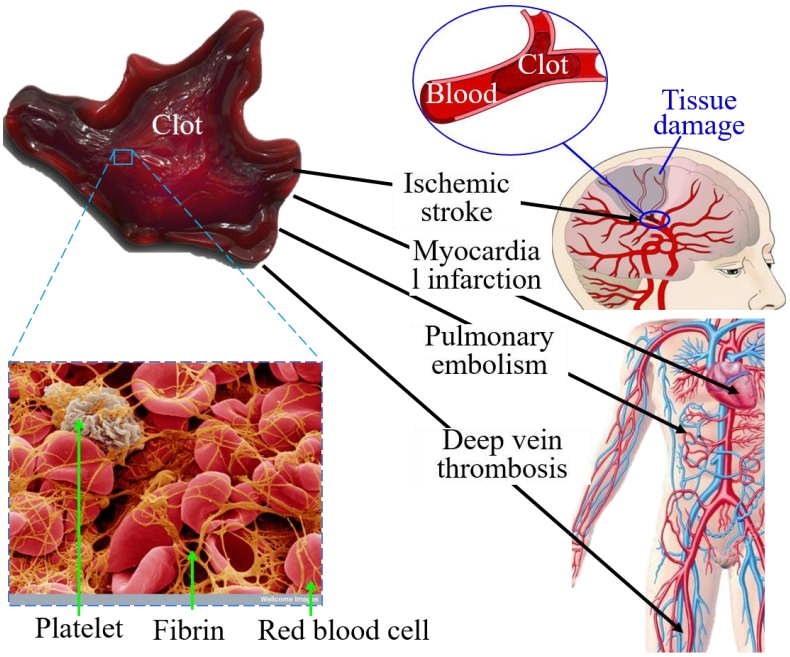

Figure 1.1 Blood clot and related diseases due to vessel occlusion.

Clots can be adversely formed inside a vessel or a heart chamber, restricting blood supply to the downstream tissue and cause cell death. Clots can also be carried by the blood flow to occlude vessels in the brain, heart, lung, or extremities, as shown in Figure 1.1, leading to ischemic stroke, myocardial infarction, pulmonary embolism (PE), or deep vein thrombosis (DVT), respectively. Clots have a significant adverse impacts to health with about 692,000 cases of ischemic stroke [3], 805,000 cases of myocardial infarction [3], and 300,000 to 600,000 cases of PE and DVT [4] in the US each year. Ischemic stroke accounts for 87% of stroke, which is the fifth leading cause of death and the leading cause of long term disability in the US [3].

Timely, complete, and minimally invasive removal of the blood clots to restore the blood flow is key for stroke treatment. Traditionally, tissue plasminogen activator (tPA) was the only medical therapy approved by the US Food and Drug Association (FDA) to dissolve clots in attempt to restore the blood flow. However, tPA has to be applied to patients within about 4.5 hours of stroke symptom onset [5] and is not effective to dissolve large clots [6]. Since 2015, catheter-based mechanical thrombectomy, an interventional procedure to retrieve clots, has been adopted in treatment [7]. Mechanical thrombectomy within 16 hours [8] and 24 hours [9] after stroke onset showed benefits in reduced morbidity after 90 days.

Current mechanical thrombectomy techniques are based on vacuum suction using a catheter tube (Figure 1.2(a)), an expanded stent (stent retriever) to pull (Figure 1.2(b)), or the combination of the suction and stent retriever (Figure 1.2(c)). The vacuum suction (Figure 1.2(a)) uses a long, thin, flexible suction catheter tube to inhale the clot. The inhaled clot can block the catheter tip and prevent further clot inhaling and the catheter is pulled back. The stent retriever uses an expanded stent to engage the clot and pull the clot out. However, the stent may cut through the clot and release clot fragments which may flow to adjacent arterial tributaries and cause new blood occlusions (embolizations). A 10% embolization rate was reported for the stent retriever [10]. To evaluate the effectiveness of mechanical thrombectomy devices, one way is to quantify the percentage of ischemic territory that achieves reperfusion after the mechanical thrombectomy procedure, graded by the modified treatment in cerebral infarction (mTICI) score: 0-3 (0 for no clot removal and 3 for complete removal) for stroke [11]. A score of mTICI = 3 is associated with the best patient outcome and is suggested to be the aim of the mechanical thrombectomy procedure [12,13]. However, the success rate to achieve complete clot removal is only 34% to 38% for suction catheters [14,15], 19% to 36% for stent retrievers [14–18], and 48%

for the combined suction catheter and stent retriever approach [19]. Detailed results of the mechanical thrombectomy device effectiveness from recent clinical trials can be found in Table 1.1. Achieving complete and safe clot removal is currently a major challenge in stroke treatment.

Table 1.1 Mechanical thrombectomy for stroke patients in recent clinical trials.

Trial	Year	*n*	Clot location	mTICI score				
				0	1	2a	2b	3
IMS III [20]	2013	434	MCA, ICA, BA	17%	9%	34%	37%	2%
MR CLEAN [16]	2015	233	MCA ICA, ACA	14%	6%	22%	35%	24%
EXTEND-IA [19]	2015	35	MCA, ICA	3%	3%	7%	38%	48%
ESCAPE [21]	2015	165	MCA, ICA		28%*		72%**	
REVASCAT [17]	2015	103	MCA, ICA	8%	2%	25%	47%	19%
DAWN [9]	2018	107	MCA, ICA		16%*		84%**	
DEFUSE 3 [8]	2018	92	MCA, ICA	11%	0	13%	57%	19%

n: patient number

MCA: middle cerebral artery

ICA: internal carotid artery

BA: basilar artery

ACA: anterior cerebral artery

* Combined percentage for mTICI = 0, 1, and 2

** Combined percentage for mTICI = 2b and 3

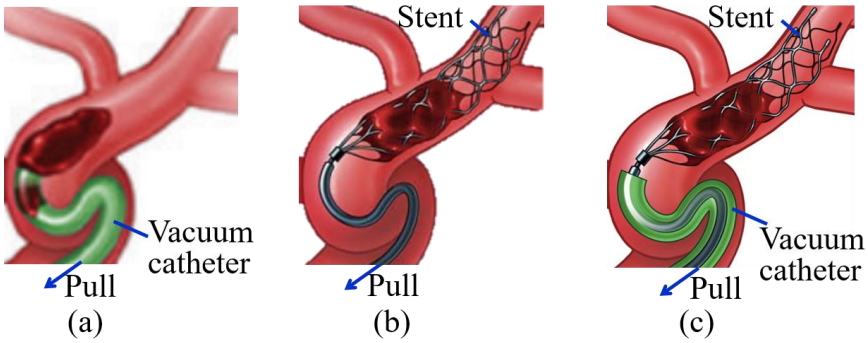

Figure 1.2 Three types of mechanical thrombectomy techniques to remove blood clots based on (a) vacuum suction, (b) stent retriever, and (c) combination of vacuum and stent.

This challenge reveals a lack of understanding of how the clots react under the mechanical load from the mechanical thrombectomy devices, which is determined by the clots' mechanical properties. The clot mechanical properties have been tested in different methods, such as: compression, rheometer, shear wave elastography, and tensile tests.

The compression test is the most commonly used way to characterize the clot mechanical properties. Different compression methods, such as confined, unconfined, and indentation, have been carried out. Slaboch et al. [22] did a confined nanoindentation test on cylindrical murine CAs using a creep loading curve. The elastic modulus and viscosity of the CA was found by an inverse finite element simulation based on Kelvin-Voigt and standard linear solid viscosity models. Xie et al. [23] did an unconfined compression test on cylindrical murine CAs. Strain and stress values were estimated to calculate the averaged elastic modulus and they found the modulus increases as the CA ages. Dempfle et al. [24] did an unconfined compression test on human CAs using the Hemodyne Hemostasis Analyzer to measure the elastic modulus. They found the elastic modulus is mainly affected by the fibrinogen concentration. Krasokha et al. [25] did a confined compression test on porcine and human CAs using a conventional compression machine and found the CAs' stiffness increases with larger strain. Other researchers have done unconfined compression tests on CAs using a dynamic mechanical analyzer to measure the elastic modulus [26–28].

The rheometer has been used to characterize the clot viscoelastic properties. The rheometer compresses the specimen by a cone/plate and the cone/plate rotates to apply a sinusoidal shear strain on the specimen, while the torque on the cone/plate is measured. From the torque value, shear stress on the specimen can be calculated and used to characterize the

elastic (storage modulus) and viscous (loss modulus) responses. Kim et al. [29] used the rheometer test to study the effect of compression on the fibrin networks on the viscoelastic properties and found the fibrin network softens at a mild compression strain and hardens at a strong compression strain. Rheometer was also used to build the constitutive models for porcine CAs [30] and the fibrin network [31].

The shear wave elastography also measures the clot viscoelastic properties by monitoring the motion response of the specimen under propagating shear waves induced by ultrasound. Huang et al.[32] measured the viscoelasticity of porcine CAs with different RBC levels and found a higher RBC level leads to lower shear modulus and this method is not accurate for viscosity measurement. Schmitt et al. [33] fitted the experimental results using five different viscoelastic models and found the Zener model is the best for porcine CAs. Malone et al. [34] found adding more thrombin increases the Young's modulus for bovine CAs.

The tensile test is different with the abovementioned test methods in that it is a destructive test and can measure the clot strength. Clot tensile test has only been investigated in two studies. Dog bone-shaped CAs were molded and pulled to get the stress-strain relation for CAs made from human and porcine whole blood [25], and bovine whole blood [34] and the clot strength was found to be 6kPa and 30 kPa, respectively.

The tensile test is a more clinically relevant engineering test but is seldomly studied and none has been carried out for clots retrieved from stroke patients. The tensile test mimics the pulling back of a suction catheter or a stent retriever against the blood flow and friction between the clot and the vessel wall. The clot tensile strength determines when the clot will fragment and create embolization. Knowing the clot tensile properties can help understand how the clot reacts under the load from the mechanical thrombectomy devices and assist in developing new devices.

In this thesis research, a cutting-based catheter was designed and built. The catheter works by inhaling the clot by vacuum pressure and then fragmenting the clot into chips using a rotating miniature cutting tool. This clot-cutting catheter eliminates the risks of embolization caused by clot fracturing outside the catheter. The feasibility of the clot-cutting catheter was validated with soft and weak CAs, but the removal of clots with high strength remains a challenge and the safety concerns exist.

1.2 Research Goal and Objectives

The goal of this study is to achieve safe and complete removal for all types of clots. To achieve this goal, four objectives are identified:

(1) Characterize the tensile properties and composition of patient clots;
(2) Guided by the known tensile properties and composition of patient clots, fabricate CAs that can mimic the patient clots;
(3) Design, manufacture, and test a miniature cutting tool and integrate the cutting tool into a clot-cutting catheter and use this device to study cutting forces;
(4) Understand the fluid behavior of the clot cutting catheter through experiments and modelling and apply the knowledge to mitigate risks of the clot-cutting catheter.

Achieving these objectives will provide engineering insights in the clot removal using mechanical thrombectomy devices to the clinicians and device manufacturers for improved complete clot removal rate and the associated better patient outcomes.

1.3 Organization of the Dissertation

The rest of this dissertation has the following organization.

Chapter 2 presents an experimental study of the retrieved clots from stroke patients. Clots' composition is quantified by histology and mechanical properties are characterized by uniaxial tensile tests. The material property and testing methodology serve as the foundation of this clot removal study.

Chapter 3 introduces the fabrication and testing of CAs. CAs are made from mixing human blood products of varied volume ratios to mimic the large range of histological composition and tensile properties of patient clots. The CAs replace the highly regulated and access-limited patient clots to serves as a valuable tool for clot removal research and mechanical thrombectomy device development.

Chapter 4 investigates the cutting mechanics using a clot-cutting catheter with a rotating miniature cutting tool. The cutting force components are measured experimentally and modelled by the SPG method.

Chapter 5 studies the fluid flow inside the clot cutting catheter. The potential risks due to the catheter fluid flow are identified and mitigation strategies are proposed.

Chapter 6 draws the conclusions and summarizes the original contributions of the dissertation. Several topics for future research are also proposed.

1.4 References

[1] Jackson SP (2006) The growing complexity of platelet aggregation. *Blood* 109(12):5087–5095.

[2] Fogelson AL, Neeves KB (2015) Fluid Mechanics of Blood Clot Formation. *Annual Review of Fluid Mechanics* 47(1):377–403.

[3] Benjamin EJ, Virani SS, Callaway CW, Chang AR, Cheng S, Chiuve SE et al. (2018) Heart disease and stroke statistics—2018 update: A report from the American Heart Association. *Circulation* 137(12):e67–e492.

[4] Beckman MG, Hooper WC, Critchley SE, Ortel TL (2010) Venous Thromboembolism: A Public Health Concern. *American Journal of Preventive Medicine* 38(4 Suppl):S495–S501.

[5] Powers WJ, Rabinstein AA, Ackerson T, Adeoye OM, Bambakidis NC, Becker K et al. (2018) 2018 guidelines for the early management of patients with acute ischemic stroke: A guideline for healthcare professionals from the American Heart Association/American Stroke Association. *Stroke* 49(3):e46–e110.

[6] Riedel CH, Zimmermann P, Jensen-kondering U, Stingele R, Deuschl G, Jansen O (2011) The importance of size successful recanalization by intravenous thrombolysis in acute anterior stroke depends on thrombus length. *Stroke* 42(6):1775–1778.

[7] Palaniswami M, Yan B (2015) Mechanical thrombectomy is now the gold standard for acute ischemic stroke: implications for routine clinical practice. *Interventional Neurology* 4(1–2):18–29.

[8] Albers GW, Marks MP, Kemp S, Christensen S, Tsai JP, Ortega-Gutierrez S et al. (2018) Thrombectomy for Stroke at 6 to 16 Hours with Selection by Perfusion Imaging. *New England Journal of Medicine* 378(8):708–718.

[9] Nogueira RG, Jadhav AP, Haussen DC, Bonafe A, Budzik RF, Bhuva P et al. (2018) Thrombectomy 6 to 24 Hours after Stroke with a Mismatch between Deficit and Infarct. *New England Journal of Medicine* 378(1):11–21.

[10] Costalat V, Lobotesis K, Machi P, Mourand I, Maldonado I, Heroum C et al. (2012) Prognostic factors related to clinical outcome following thrombectomy in ischemic stroke (RECOST Study). 50 patients prospective study. *European Journal of Radiology* 81(12):4075–4082.

[11] Zaidat OO, Yoo AJ, Khatri P, Tomsick TA, Von Kummer R, Saver JL et al. (2013) Recommendations on angiographic revascularization grading standards for acute ischemic stroke: A consensus statement. *Stroke* 44(9):2650–2663.

[12] Kleine JF, Wunderlich S, Zimmer C, Kaesmacher J (2017) Time to redefine success? TICI 3 versus TICI 2b recanalization in middle cerebral artery occlusion treated with thrombectomy. *Journal of NeuroInterventional Surgery* 9(2):117–121.

[13] Dargazanli C, Fahed R, Blanc R, Marnat G, Saleme S, Costalat V et al. (2018) Modified thrombolysis in cerebral infarction 2C / thrombolysis in cerebral infarction 3 reperfusion should be the aim of mechanical thrombectomy. *Stroke* 49(5):1189–1196.

[14] Lapergue B, Blanc R, Gory B, Labreuche J, Duhamel A, Marnat G et al. (2017) Effect of endovascular contact aspiration vs stent retriever on revascularization in patients with acute ischemic stroke and large vessel occlusion: The ASTER randomized clinical trial. *JAMA* 318(5):443–452.

[15] Turk A, Mocco J, SIddiqui A (2018) COMPASS Trial: A comparison of direct aspiration vs. stent retriever as a first approach. in: Int. Stroke Conf., Los Angeles, CA.

[16] Berkhemer OA, Fransen PSS, Beumer D, Berg LA, van den Lingsma HF, Yoo AJ et al. (2015) A randomized trial of intraarterial treatment for acute ischemic stroke. *New England Journal of Medicine* 372(1):11–20.

[17] Jovin TG, Chamorro A, Cobo E, de Miquel MA, Molina CA, Rovira A et al. (2015) Thrombectomy within 8 Hours after symptom onset in ischemic stroke. *New England Journal of Medicine* 372(24):2296–2306.

[18] Albers GW, Marks MP, Kemp S, Christensen S, Tsai JP, Ortega-Gutierrez S et al. (2018) Thrombectomy for stroke at 6 to 16 hours with selection by perfusion imaging. *New England Journal of Medicine* 378(8):708–718.

[19] Campbell BCV, Mitchell PJ, Kleinig TJ, Dewey HM, Churilov L, Yassi N et al. (2015) Endovascular therapy for ischemic stroke with perfusion-imaging selection. *New England Journal of Medicine* 372(11):1009–1018.

[20] Broderick JP, Palesch YY, Demchuk AM, Yeatts SD, Khatri P, Hill MD et al. (2013) Endovascular Therapy after Intravenous t-PA versus t-PA Alone for Stroke. *New England Journal of Medicine* 368(10):893–903.

[21] Goyal M, Demchuk AM, Menon BK, Eesa M, Rempel JL, Thornton J et al. (2015) Randomized Assessment of Rapid Endovascular Treatment of Ischemic Stroke. *New England Journal of Medicine* 372(11):1019–1030.

[22] Slaboch CL, Alber MS, Rosen ED, Ovaert TC (2012) Mechano-rheological properties of the murine thrombus determined via nanoindentation and finite element modeling. *Journal of the Mechanical Behavior of Biomedical Materials* 1075–86.

[23] Xie H, Kim K, Aglyamov SR, Emelianov SY, O'Donnell M, Weitzel WF, et al. (2005) Correspondence of ultrasound elasticity imaging to direct mechanical measurement in aging DVT in rats. *Ultrasound in Medicine and Biology* 31(10):1351–1359.

[24] Dempfle C-E, Kälsch T, Elmas E, Suvajac N, Lücke T, Münch E et al. (2008) Impact of fibrinogen concentration in severely ill patients on mechanical properties of whole blood clots. *Blood Coagulation & Fibrinolysis : An International Journal in Haemostasis and Thrombosis* 19(8):765–770.

[25] Krasokha N, Theisen W, Reese S, Mordasini P, Brekenfeld C, Gralla J et al. (2010) Mechanical properties of blood clots - A new test method. *Materialwissenschaft Und Werkstofftechnik* 41(12):1019–1024.

[26] Chueh JY, Wakhloo AK, Hendricks GH, Silva CF, Weaver JP, Gounis MJ (2011) Mechanical characterization of thromboemboli in acute ischemic stroke and laboratory embolus analogs. *AJNR American Journal of Neuroradiology* 32(7):1237–1244.

[27] Robinson RA, Herbertson LH, Das SS, Malinauskas RA, Pritchard WF, Grossman LW (2013) Limitations of using synthetic blood clots for measuring in vitro clot capture efficiency of inferior vena cava filters. *Medical Devices: Evidence and Research* 649–57.

[28] Ashton JH, Vande Geest JP, Simon BR, Haskett DG (2009) Compressive mechanical properties of the intraluminal thrombus in abdominal aortic aneurysms and fibrin-based thrombus mimics. *Journal of Biomechanics* 42(3):197–201.

[29] Kim O V., Litvinov RI, Weisel JW, Alber MS (2014) Structural basis for the nonlinear mechanics of fibrin networks under compression. *Biomaterials* 35(25):6739–6749.

[30] van Kempen THS, Donders WP, van de Vosse FN, Peters GWM (2016) A constitutive model for developing blood clots with various compositions and their nonlinear viscoelastic behavior. *Biomechanics and Modeling in Mechanobiology* 15(2):279–291.

[31] van Kempen THS, Peters GWM, van de Vosse FN (2015) A constitutive model for the time-dependent, nonlinear stress response of fibrin networks. *Biomechanics and Modeling in Mechanobiology* 14(5):995–1006.

[32] Huang CC, Chen PY, Shih CC (2013) Estimating the viscoelastic modulus of a thrombus using an ultrasonic shear-wave approach. *Medical Physics* 40(4):042901.

[33] Schmitt C, Hadj Henni A, Cloutier G (2011) Characterization of blood clot viscoelasticity by dynamic ultrasound elastography and modeling of the rheological behavior. *Journal of Biomechanics* 44(4):622–629.

[34] Malone F, McCarthy E, Delassus P, Fahy P, Kennedy J, Fagan AJ et al. (2018) The mechanical characterisation of bovine embolus analogues under various loading conditions. *Cardiovascular Engineering and Technology* 9(3):489–502.

CHAPTER 2
ANALYSIS OF HUMAN EMBOLI AND MECHANICAL THROMBECTOMY FORCES IN LARGE VESSEL OCCLUSION STROKE

2.1 Introduction

Mechanical thrombectomy using catheter−based device to remove a clot causing a large vessel occlusion (LVO) in the anterior cerebral circulation became a standard of care in 2015 after multiple randomized clinical trials demonstrated statistical significant improvements in clinical outcome [1]. To date, two devices have been approved by the FDA [2]: 1) suction catheters that employ large−bore catheters to aspirate the clot and 2) stent retrievers that are deployed across the clot and then pulled into an suction catheter dragging the embolus “en bloc”.

Employing currently available devices, “successful” recanalization, or reperfusion in greater than 50% of the target ischemic territory, or mTICI score of 2b and 3 [3], is routinely achieved in 80−90% of cases leading to improved patient outcomes. However, complete recanalization (mTICI=3), which is known to be associated with the best neurological outcome, is achieved only in less than 50% of patients [4]. In addition, with these devices distal embolization can be seen causing macro and microvascular occlusions [5,6]. Furthermore, the procedural times are still unacceptably long given the high pace of neuronal depth under ischemia [7,8], and multiple passes may be required to remove the clot and cause focal vascular injury in the arterial territory [9].

To gain further understanding of the complex clot deformation in tensile pulling and provide biomechanical explanations for failure modes of current thrombectomy devices and opportunities for improvement, in this study we empirically analyzed the retrieval process of clots causing LVO in a testbed we constructed with anatomically accurate arterial phantoms and

physiological flow and pressures. We observed that stent and suction catheters subjected the CAs to tensional forces leading to elongation, fracture and material removal. Therefore, it was determined that a destructive tensile test of patient-derived clots would be a clinically relevant analysis to provide data on clot elongation and fracture properties and measure material strength of clots. To this end, we built a test platform and conducted uniaxial tests on clots removed from patients with LVO strokes. Then, histological analysis of the clots with structural quantification was performed to correlate the tensile properties to the histologic composition of clots and to help generate CAs with representative tensile strength and histological composition which can be used for testing of future mechanical thrombectomy technologies.

The purpose of this study was to gain an understanding of the forces driving the complex interaction between clots and stroke thrombectomy devices by analyzing retrieval in a middle cerebral artery bifurcation model and evaluating the mechanical forces and histological composition of clots obtained from patients with stroke.

2.2 Materials and Methods

2.2.1 Testbed of Mechanical Thrombectomy Devices

A free-standing glass phantom made of borosilicate of the ICA, ACA, and MCA reconstructed from the computed tomography (CT) scan of a stroke patient (Farlow's Scientific Glassblowing, Grass Valley, CA) was used to visualize the clot retrieval process. The phantom was connected to a hydraulic system composed of a peristaltic pump (Model 77601-10; Masterflex, Gelsenkirchen, Germany), tubing and variable resistance escape valves as previously described by our group [10].

CAs were generated by mixing plasma and RBC from human blood with a volume ratio of 9:1. The calcium chloride solution (2.3 wt%) was added to the mixture with a volume ratio of 1:10 to induce coagulation [11,12]. The mixture then rested at 37°C for 90 minutes in a centrifuge tube with a diameter of 15 mm to form a CA. The CA was then removed from the tube and sectioned into 5 mm long fragments. The CA was then injected into the tubing system

through an injection port (with a 5mm diameter to prevent any tissue deformation) and carried distally by physiological flow with flow rate of 265 mL/min [13] into the MCA bifurcation.

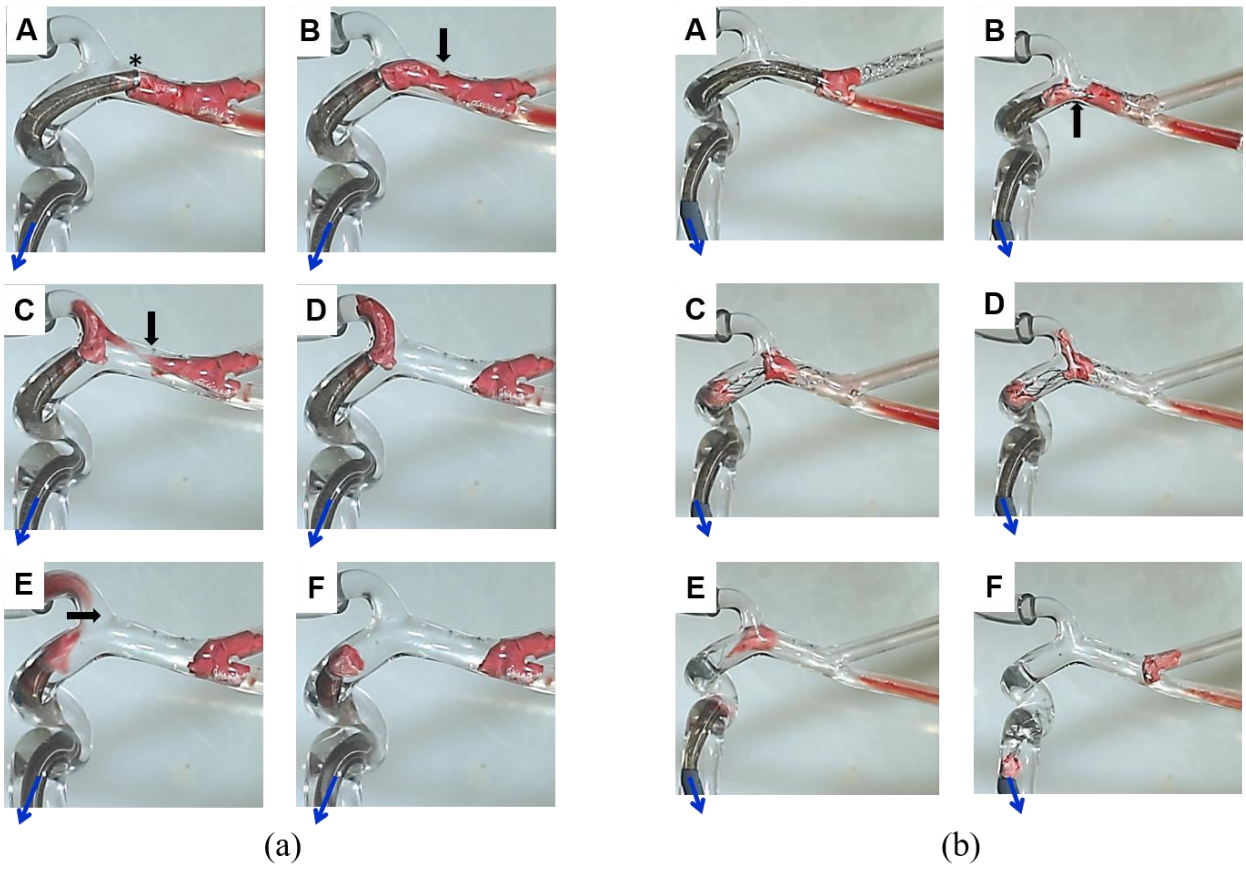

Figure 2.1 Mechanical thrombectomy in a cerebrovascular simulator. A glass phantom of the ICA and major intracranial arteries was pressurized with saline solution and a CA embolized into the MCA. Then, mechanical thrombectomy was conducted with (a) suction catheter and (b) combining suction catheter with stent retrievers. Asterisk in A indicates the clot entering the suction catheter under vacuum (engagement segment). Blue arrows indicate the pulling direction.

Mechanical thrombectomy of the CAs was conducted by: 1) direct suction first pass technique (ADAPT) employing suction catheter (ACE 68; Penumbra, Alameda, CA) (Figure 2.1(a)) [13]; 2) continuous suction prior to intracranial vascular embolectomy (CAPTIVE) with Solitaire™ Platinum revascularization device (Medtronic) and suction catheter (ACE 68; Penumbra, Alameda, CA) (Figure 2.1(b)) [14]. Thrombectomy procedures were performed 10 times which each technique and videos recorded for analysis by team of mechanical engineers and neurointerventionalists including radiologist and neurosurgeons. The forces involved in the

removal process were analyzed, described and categorized. The material response of CAs to the action of thrombectomy device was recorded and analyzed. The number of passes needed to recanalize the obstructed artery was quantified. During the test, clot fragments were produced from interacting with the devices and were collected in a collection canister connected to the outflow ports of the glass phantom. After each pass of a mechanical thrombectomy, the clot fragments were collected from the canister and placed next to a ruler. A photo of each clot fragment was taken with a camera. The images were then processed using the image processing software Fiji v. 2.0.0 [15]. The area was calculated by tracing the outline of each clot fragment. The equivalent diameter was then calculated assuming a circular shape. Clot fragments smaller than 1 mm were excluded.

2.2.2 Patient Clot Collection

After institutional approval (HUM00133468), clots were prospectively collected from patients undergoing thrombectomy from October 2017 to December 2018 in the Comprehensive Stroke Center at the University of Michigan. In our institution, the combination of a stent retriever and an suction catheter using the CAPTIVE technique is the standard employed [16], as shown in Figure 2.2. During this period, 75 thrombectomy procedures for LVO were included in this study and 37 clots removed from 20 patients were of sufficient size (at least 10 mm in length and 3 mm in diameter) for tensile test. The remaining clots were too small for testing (the majority consisted of small fragments along the tines of the stent) or the clot material could not be located despite meticulous inspection of stent retriever, suction catheter, suction tubing, and blood collection canister. Upon collection, clots were maintained in nonheparinized normal saline solution at 4°C until testing, which was conducted within 24 hours after the mechanical thrombectomy procedure.

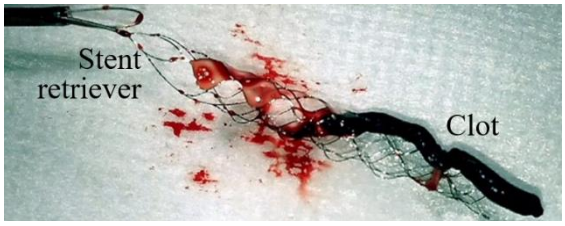

Figure 2.2 A clot taken out by a stent retriever.

2.2.3 Tensile Test Setup

The tensile test was carried out using a customized tensile test machine built for this study, as shown in Figure 2.3(a). The machine consists of a computer-controlled linear stage (200cri; Siskiyou, Grants Pass, Oregon) to pull the clots at a constant speed and a force sensor (Gamma; ATI Industrial Automation, Apex, North Carolina) to measure the tensile force (F). The clot was gripped by two hemostats. One hemostat was fixed to a linear stage and the other hemostat was fixed to a stationary force sensor. The clot was pulled at a rate of 0.2 mm/s to neglect the viscoelastic effect until breaking. The sampling rate of the tensile force data was 50 Hz. A moving average filter of 10 data points was applied to reduce the noise. The noise may come from electromagnetic interference on the force sensor and the and vibrations from the linear stage.

Figure 2.3(b) shows an example pulling force measurement for clot #2A (in Table A1). The pulling force rises as pulling distance increases. The clot deforms until the fracture after 11 mm of tensile pulling. Two video cameras (α6000; Sony, Tokyo, Japan) recorded digital images of the deformed clot from top and side at 30 frames per second. Images from two cameras at the same time instance could be used to estimate the cross-sectional area of clot during tensile testing. Two fiducials, as shown in Figure 2.3(a), were added to both ends of the clot by gently touching the clot with a needle tube (dipped in silicone pigment beforehand) before pulling to track the elongation of the clot.

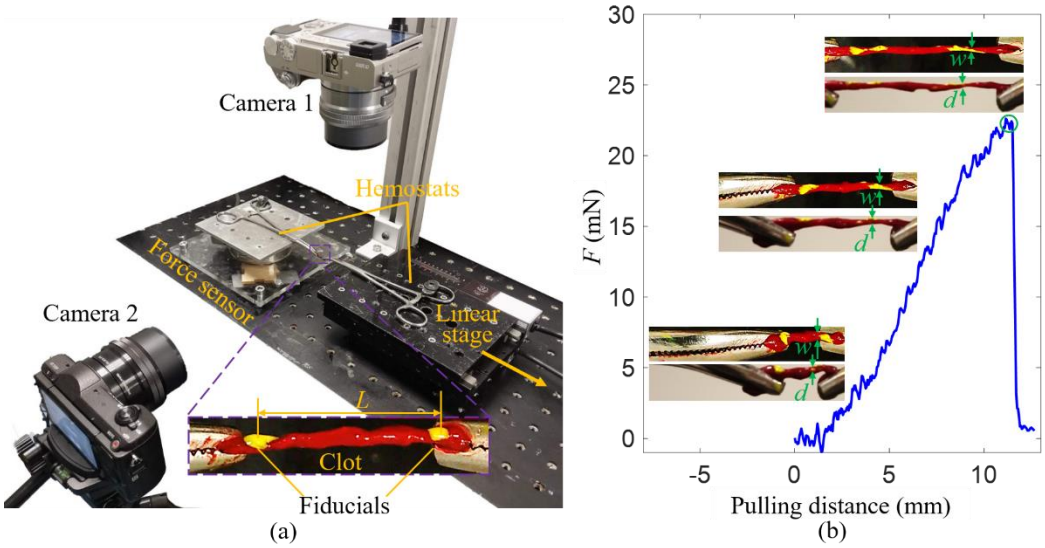

Figure 2.3 (a) Tensile test setup and (b) tensile test force measurement for clot #2A.

To quantify the clots tensile properties, true stress (σ) and engineering strain (ε) were calculated. The true stress is the loading on a material per unit area caused by force (i.e., suction catheter and stent retriever related pulling, and, in our case, the hemostats' pull), which then causes the material to deform (in our case, to elongate until the clot fractured). The engineering strain quantifies the elongation of the clot.

The true stress σ was calculated by dividing the measured tensile force F over the clot cross-sectional area A. The A was estimated at the location where the clot fractured, as indicated by the green arrows in Figure 2.3(b). At this location, the widths of clot were measured by the cameras from the top and side, denoted as w and d, respectively, using the edge-detection algorithm in MATLAB (v2017b; MathWorks®, Natick, Massachusetts) with an uncertainty about 40 μm. For clots that fractured in different stages and locations, the location where w and d were tracked changed accordingly. Assuming the clot has an elliptical cross section, $A = \pi wd/4$ and the true stress σ is:

$$\sigma = \frac{4F}{\pi wd} \tag{2.1}$$

At fracture, the clot has an ultimate tensile stress σ_{ut}.

The engineering strain ε was calculated based on the distance (L) between two fiducials. L was estimated using an open-source image processing software (Kinovea v0.8.15). The L_o was defined as the distance between the two fiducials when the pulling force just rose to 2 mN. This value was selected due to the about 1mN uncertainty in the force measurement. The engineering strain ε is calculated as:

$$\varepsilon = \frac{L}{L_0} - 1 \tag{2.2}$$

At fracture, the clot has an ultimate tensile strain ε_{ut}.

2.2.4 Quantification of Clot Composition

After tensile testing, the clots were fixed in 10% neutral buffered formalin solution, embedded in paraffin, and sliced using a microtome at 5 μm slice thickness. Slides with 3 to 5 cuts were stained with hematoxylin and eosin (H&E) to highlight the RBC from the fibrin matrix [11,17–23], and immunostained with CD61 (anti-ITGB3 antibody (HPA027852; Atlas Antibodies, Stockholm, Sweden)) for platelet percentage [20]. The stained slides were scanned by a microscope (BX51; Olympus, Tokyo, Japan) at 40× magnification, and the images were taken with a digital camera (DP70; Olympus, Tokyo, Japan) at 1600 × 1200 resolution. The H&E and CD61 images were processed using ImageJ (v1.52; National Institutes of Health) to count the dark red and dark brown pixels over the total pixels occupied by the clot sample to determine the percentages of RBC and platelets, as shown in Figures 2.4 (a) and (b), respectively. The rest was assumed to be fibrin [20]. For clot specimens with multiple fragments, the composition percentages were calculated using images from all fragments. The quantification was done by a trained graduate student supervised and by a board-certified pathologist with specialization in cardiovascular diseases. The graduate student and the pathologist were unaware of the patient's medical history and blinded to the tensile testing results.

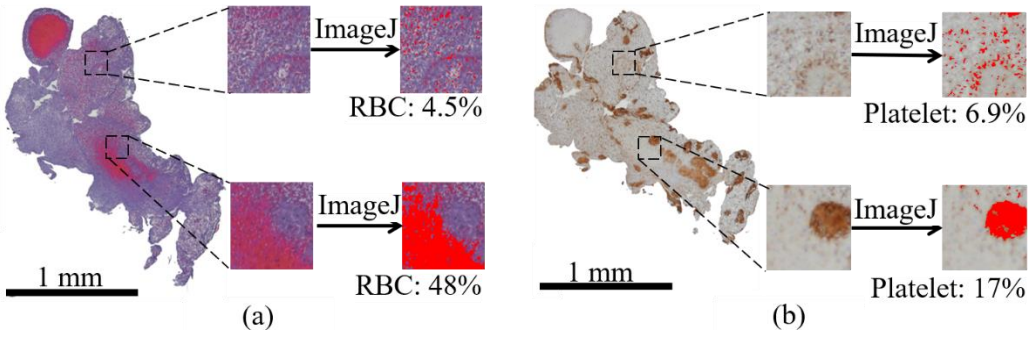

Figure 2.4 Microscopic images and quantification method of slides stained with (a) H&E and (b) CD61.

2.2.5 Statistical Analysis

To understand how clot composition affects clot strength, two-sided Pearson correlation coefficient (r) was calculated. This method was used by Niesten et al. [23] to analyze the effect

of patient clot composition on clot attenuation. The correlations between the compositions (RBC, fibrin, and platelets) and the ε_{ut} and σ_{ut} were calculated. ANOVA test was used to test if the number of fracture (n_f) has anything to do with the clot histological composition. All statistical analyses were carried out using SPSS (v24.0; IBM, Chicago, IL). $p < 0.05$ was considered statistically significant.

2.3 Results

2.3.1 Simulated Mechanical Thrombectomy in the Testbed

The technique described in Section 2.2.1 allowed reproducible lodging of a CA into the MCA bifurcation leading to a complete occlusion resistant to fragmentation by the physiological flow. Mechanical thrombectomy of the CAs was successfully conducted employing ADAPT (Figure 2.1(a)) and CAPTIVE (Figure 2.1(b)) techniques for 10 times each.

The forces involved in the removal process were analyzed, described and categorized into the retrieval forces, resistance forces and emboligenic forces, as shown in Figure 2.5. The retrieval forces favor retrograde removal of the clots and include tensional forces applied by the devices on the clots (vacuum by suction catheters and/or linear pull of stents and catheters) and intravascular pressure distal to the site of the occlusion. The resistance forces refer to the ability of the clots to resist change and include static friction and adhesion at the clot/vascular surface interface, mechanical strength of the clot opposing the material intruding into the branching arteries to deform and enter into the main artery and then into the suction catheter for removal, and the arterial pressure proximal to the obstruction, as shown in Figure 2.5(a). If the retrieval forces overcome resistance forces, at least a part of the clot will become disimpacted leading to a stage where emboligenic forces favor downstream migration of clot fragments under reconstituted flow conditions, and include kinetic friction at the clot/vascular surface interface and hemodynamic stress comprising of shear and pressure at the clot/blood interface, as shown in Figure 2.5(b).

During ADAPT technique, the suction catheters were advanced to the proximal edge of the CAs and connected to the vacuum source (−650 mmHg) for 5 minutes before withdrawal.

During this time, it was observed the CAs entered the lumen of the suction catheter for few millimeters and then remain in a stable position. The distal region of the suction catheter occupied with CAs was called engagement segment (asterisk in Figure 2.1(a)). During suction catheter withdrawal, CAs were observed to elongate, decrease in diameter and undergo multistage fracture leading to embolization into the same vascular territory and other arterial branches. In the 10 procedures performed, we observed 13 clot fragments in total with an average of 1.3 clot fragments per intervention, and an average size of 5.95mm (SD 6.06 mm). An average of 1.5 attempts (SD 0.5) with the suction catheter were used to recanalize the MCA. During the clot removal, the major retrieval force was found to be uniaxial tensile force at the engagement segment leading to the CAs' elongation and thinning to overcome the resistance forces at the CA/phantom interface, mostly consisting of static friction and adhesion and differential pressure across the CA. After disimpaction of the CA and at least partial recanalization of the lumen, emboligenic forces included kinetic friction of the CA to the glass phantom surface and hemodynamics forces (shear and flow) of the saline solution over the CA surface.

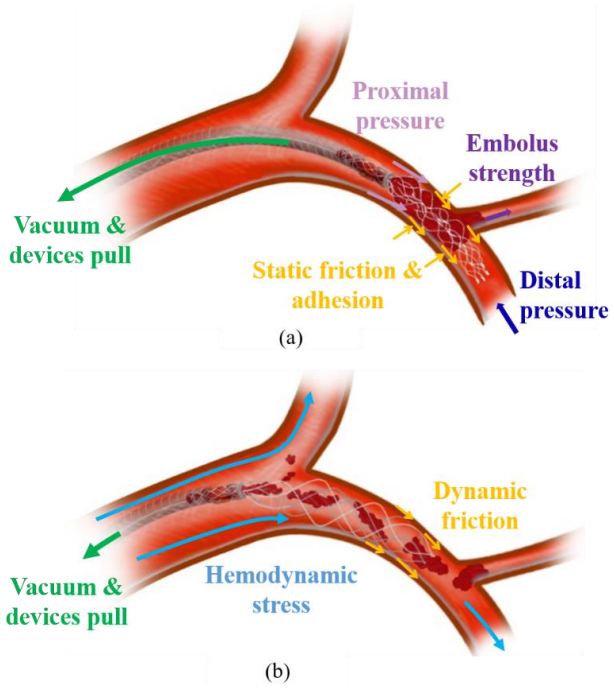

Figure 2.5 Interplay of forces involved in the removal of clots in LVO: (a) during clot engagement and initial device withdrawal and (b) after clot disimpaction and removal.

During CAPTIVE technique, the stent was deployed centered in the CA with at least 1/3 of the stent distal to the CA and 1/3 inside the catheter (Figure 2.1(b)). The stent had enough radial force to incorporate into the CA mass and had good apposition to the phantom wall. The suction catheter was then advanced until contacting the CA and connected to vacuum for 5 minutes before withdrawal. Stent pull back was performed after stent deployment under full vacuum and simultaneously to the suction catheter to avoid shearing of CA at the catheter tip. During the clot removal process, the tensional forces dislodged the CA from the MCA bifurcation with associated CA elongation, thinning and fracture. Stent integration to the CA was weaker at the branching point with stent deployment confined to the diameter of the distal and smaller lumen, leaving CA substance outside the stent tines. This CA substance still experienced elongation and fracture during device withdrawal and had exposure to the hemodynamic forces and friction to the phantom wall leading to high emboligenic propensity. These mechanisms were consistently associated with overall decrease in grasp and total retrieval forces concurrent to increase in pro-emboligenic forces due to restored flow through the lumen leading to incomplete clot removal and iatrogenic embolization. The segment of the CAs that was most consistently removed and less likely to embolize was at the interface between the suction catheter and the stent. In the 10 procedures performed, we observed 19 clot fragments, or 1.9 fragments per intervention (SD 0.7), with an average size of 5.88mm (SD 6.15 mm). An average of 1.9 passes (SD 0.7) of the devices were needed to recanalize the MCA.

In summary, this testbed-based experiments showed that the stent retriever and the suction catheter apply stress in the form of uniaxial tensile forces to overcome resistance forces and mobilize the clots. Clots respond with elongation and fracture concurrent to increase of pro-emboligenic forces, leading to a status highly prone to release of fragments and downstream embolization. This phenomenon leads to incomplete recanalization and iatrogenic embolization.

2.3.2 Clot Tensile Test and Histology Results

Mechanical analysis of 16 clots retrieved from 11 stroke patients with LVO were successfully performed in a quasi-static uniaxial tensile test custom-made platform as described in Section 2.2.3. Data derived from 21 specimens were not included in the analysis as clot fracture happened at a hemostat clamp due to concentrated stress (see below) or due to slipping off from the hemostatic clamp during tensile tests invalidating repeat testing.

Four fracture patterns, as shown in Figures 2.6(a) to (d), were identified for the clot in tensile test:

1) Focal fracture: focal thinning between the two hemostat tips that proceeds final fracture with dissociation;
2) Multi-focal fracture: multifocal thinning and multifocal fracture between the two hemostat tips associated with drop in pulling force that increases with continued pulling;
3) Cavitated fracture: cavity generated within the clot between the two hemostat tips and enlarged associated with drop in puling force that increases with continued pulling;
4) Stress concentrated fracture: focal tearing at the tip of the hemostats where the clot is clamped. This is due to the locally high but unknown stress generated by the clamping and therefore the test results were excluded from reporting the stress-strain result.

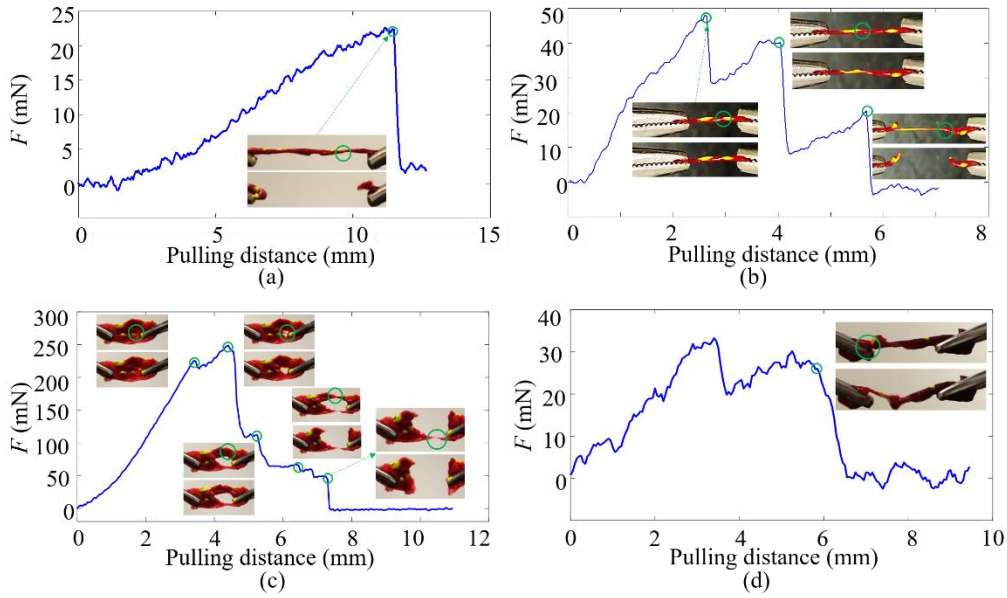

Figure 2.6 Patterns of fracture: (a) focal, (b) multifocal, (c) cavitied, and (d) stress concentrated. The fracture locations are indicated by green circles.

Figures 2.7(a)-(c) show the clots tensile stress-strain tensile test and histology results for cardioembolic, atherogenic, and cryptogenic clots, respectively.

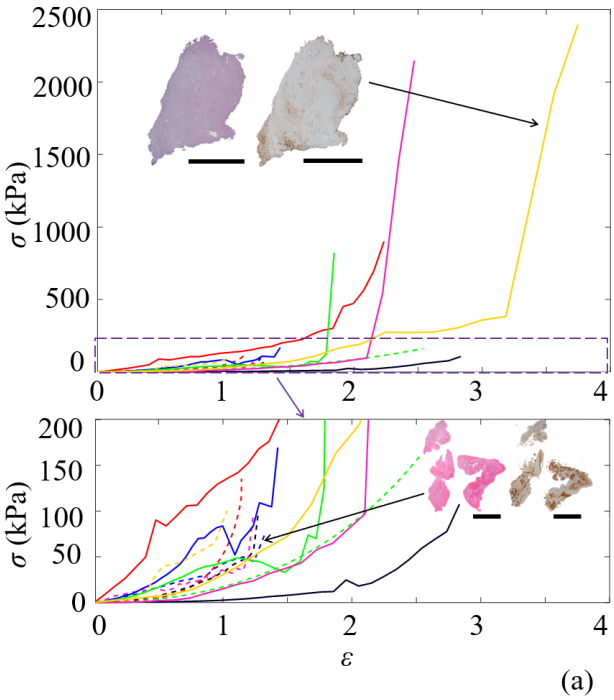

Clot #	Mechanical test			Histology		
	ε_{ut}	σ_{ut} (kPa)	n_f	RBC (%)	Fibrin (%)	Platelets (%)
1	1.3	76	1	90	0	10
2A	1.1	135	1	89	2	9
3	2.5	161	1	91	2	7
2B	1.3	97	1	79	17	4
4	1.2	98	1	69	29	2
5	1.4	170	3	29	37	34
6	2.2	901	2	29	65	6
2C	1.0	101	1	15	68	17
2D	1.8	823	5	5	81	13
2E	2.8	108	2	1	84	16
7	2.5	2148	2	2	88	10
8	3.8	2396	3	1	95	4

Clot #	Mechanical test			Histology		
	ε_{ut}	σ_{ut} (kPa)	n_f	RBC (%)	Fibrin (%)	Platelets (%)
9	3.6	63	2	49	0	51
10A	4.9	123	3	44	0	56
10B	3.1	685	2	16	59	25

Clot #	Mechanical test			Histology		
	ε_{ut}	σ_{ut} (kPa)	n_f	RBC (%)	Fibrin (%)	Platelets (%)
11	3.1	572	3	71	7	22

Figure 2.7 Results from the uniaxial tensile test for clots categorized as: (a) cardioembolic, (b) atherogenic, and (c) cryptogenic. Scale bar = 1 mm.

Clots causing LVO strokes are highly heterogeneous, both mechanically and histologically, from patient to patient and within the same patient (e.g. clots #2A to #2E). Mechanically, clots have a large range of ultimate tensile strain, with 1.05 to 4.89 ε_{ut}, and 63 to

2396 kPa σ_{ut}. Histologically, clots have 0.45% to 91% RBC, 0 to 95% fibrin, and 1.7% to 56% platelets. The strongest clot encountered in our sample was related to a left ventricular assist device, with ε_{ut} of 3.75 and σ_{ut} of 2396 kPa. For all the clots, the stress on the clots increases with strain and increases faster as the strain becomes larger. Clots with higher fibrin percentage (clots #6, #7, and #8) have much higher σ_{ut} compared to the other clots (i.e. can tolerate higher loads).

Among the 16 clots, 12 were from LVO strokes related to heart sources (cardioembolic), 3 were from LVO strokes related to carotid artery disease (atherogenic), and 1 was related to unknown etiology (cryptogenic). The cardioembolic clots had 1.14 to 3.75 (2.08±0.78) ε_{ut} and higher σ_{ut} of 76 to 2396 kPa (601±833 kPa). The atherogenic clots had 3.05 to 4.89 (3.83±0.95) ε_{ut} and 63 to 685 kPa (290±343 kPa) σ_{ut}. The crypogenic clot had ε_u of 3.1 and σ_{ut} of 572kPa.

Ten clots (62% of the clots), represented by solid lines in Figures 2.7(a)-(c) have multiple fractures ($n_f > 1$) during tensile test, with a maximum of $n_f = 5$ (clot #2D) and average of $n_f = 2.7$. These clots have 1.42 to 4.89 (2.91±1.00) ε_{ut}, 63 to 2396 kPa (799±838 kPa) σ_{ut}, 0.5% to 71% (23%±25%) RBC, 0 to 95% (53%±39%) fibrin, and 3.5% to 56% (24%±18%) platelets. The multiple fracture of the clots is due to the clots' heterogeneity and is reflected by the abrupt changes of the slope for the stress-strain curves, as shown in Figures 2.6(a)-(c). The rest six clots (38% of the clots) have single or focal fracture ($n_f = 1$) with 1.14 to 2.54 (1.64±0.54) εut, 76 to 161 kPa (111±31 kPa) σut, 15% to 90% (72%±29%) RBC, 0 to 68% (20%±26%) fibrin, and 1.7% to 17% (8.1%±5.2%) platelets. Based on one-way ANOVA test, clots with multiple fractures have higher ε_{ut} ($p = 0.013$). This is due to the multiple local tearing of the clots yields larger elongation before fracture compared to those with single or focal fracture. The ANOVA test also shows clots with multiple fractures have higher σ_{ut} but it's not as statistically significant ($p = 0.068$).

Table 2.1 shows the results of Pearson correlation analysis among clot composition (RBC, fibrin, and platelets), σ_{ut}, and ε_{ut} for the 16 patient clots. This shows:

1) The fibrin percentage is strongly ($|r| \geq 0.6$) and negatively correlated with the RBC percentage ($p < .001$);

2) The ε_{ut} is strongly and positively correlated with the platelet percentage ($p = 0.012$). Therefore, platelet rich clots tend to elongate more when under tension;
3) The σ_{ut} is strongly and positively correlated with the fibrin percentage ($p = 0.005$). Therefore, RBC-rich clots tend to fracture at lower loads than fibrin-rich clots.

Table 2.1 Correlation analysis results of clot composition and strength (n = 16).

	RBC (%)		Fibrin (%)		Platelets (%)	
	r	*p*	*r*	*p*	*r*	*p*
RBC (%)	-	-	−0.897	< .001***	−0.108	.691
Fibrin (%)	−0.897	< .001***	-	-	−0.343	.193
Platelets (%)	−0.108	.691	−0.343	.193	-	-
ε_{ut}	−0.274	.304	−0.011	.969	0.608	0.012*
σ_{ut} (kPa)	−0.565	0.023*	0.670	0.005**	−0.305	.251

* $p < 0.05$; ** $p < 0.01$; *** $p < 0.001$

2.4 Discussions

This study was conducted to gain further understanding of the forces involved in the complex interaction between clots and current stroke thrombectomy devices. We found the main force driving clot removal by suction catheters and stent retrievers to be uniaxial tension. In the phantom, this force generated CA deformation including elongation, thinning, fracture and embolization during removal. Uniaxial tensile testing of patients' clots revealed similar elongation under tension and differential fracture patterns including single focal fracture, multifocal fractures, cavitated fracture and stress concentrated fracture. The patient clots were mechanically and histologically highly variant. The ultimate tensile stress of the clots increases with fibrin percentage and decreases with higher RBC and platelet percentages.

For the suction catheters, if clots are soft, they will deform and enter the catheter lumen and will be removed exclusively by intra-catheter elongation and fracture. In our study, we attempted to reproduce this condition, but we could not draw meaningful data as this type of clots repeatedly fragmented upon introduction in the pressurized phantom and fully migrated

downstream to the collection canister. The CAs that withstood the flow of our anatomically and physiologically accurate phantoms did enter the distal most 5-10 mm of the suction catheter at full vacuum, but then clogged the catheter (Figures 2.1(a) and 2.8(a)). This phenomenon, which is commonly observed in clinical practice and explains the need for multiple attempts and catheter unclogging, may be mechanistically due to accumulation of static friction at the catheter tip that overwhelms vacuum power. At this point, withdrawal of the catheter exerts linear tension forces at the clot between the engagement segment and the clot/vascular surface interface. If the clot is stronger than total resistance forces, it will eventually disengage from the vasculature and it will be removed. In this process, it will elongate and become thinner, undergoing one or more fractures and possibly fragmentation, leading to recoil back to the obstructed artery or cause iatrogenic embolization (Figure 2.8(b)). This was the recurrent failure mechanism observed in thrombectomy procedure in our model and likely to occur in the clinical settings.

In a similar fashion, the current stent retriever can successfully remove clots from an artery when the stent integrates sufficiently to the clot to exert a linear tensile force greater than the overall resistance forces. For this to happen, the clot must be mechanically strong and homogeneous enough to resist the tensile stress and the cutting forces of the stent tines during pulling (Figure 2.8(c)). Even with good integration of the clot with the stent tines, pulling of the stent will likely lead to clot elongation and fracture first in the weakest regions, followed by fracture in stronger regions along with increased stress leading to uncontrolled and multifocal fragmentation. This may lead to disengagement of the clot from the stent and fragmentation downstream (Figure 2.8(d)). This process is likely prevalent in the regions of the clots contacting the stent tines, both due to a cutting phenomenon and stress concentration during pulling, and at branching point where subtotal stent deployment compromises clot/device interaction as showed in our analysis. This finding may explain the occurrence of macroembolization in the same or new vascular occlusion after stent retriever use and suggests that microembolization to the same vascular bed is a common phenomenon despite successful angiographic recanalization. Iatrogenic embolization was consistently observed during thrombectomy procedures in our model and was the main driver of incomplete recanalization. In addition, these results may support the use of a balloon guide catheter to arrest and reverse flow

during pulling of the stent retriever to minimize distal embolization, unless this maneuver would lead to vessel collapse which is a topic for debate.

To date, most work dedicated to the analysis of clots causing stroke has concentrated on histological characterization [20,23–25]. Although valuable, histology *per se* is a limited proxy of mechanical strength and does not provide information related to the dynamic interaction of the clot and thrombectomy device when retrieval forces are applied. To gain further understanding of the complex mechanical behavior of clots, in the past different testing methods have been used including compression [26,27], rheometer [28–31], and shear wave elastography [32]. These tests characterize the clot elastic modulus and viscoelastic properties, defining deformation of the clot under mechanical load. However, these mechanical features are not the primary drivers of current thrombectomy devices which are designed to "pull" the clots. Only two papers are available in the literature describing the tensile stress-strain relationships of CAs made from human and porcine whole blood [33] and bovine whole blood [34]. The strength of these CAs were 6 kPa and 30 kPa, respectively, about 80 times weaker than some of the samples analyzed in our cohort, raising questions about the external validity (and generalization to clinical scenarios) of the results of thrombectomy devices tested with these CAs. In addition, our data show that patient clots are mechanically and structurally heterogeneous, limiting the value of tensile analysis of bench-generated CAs.

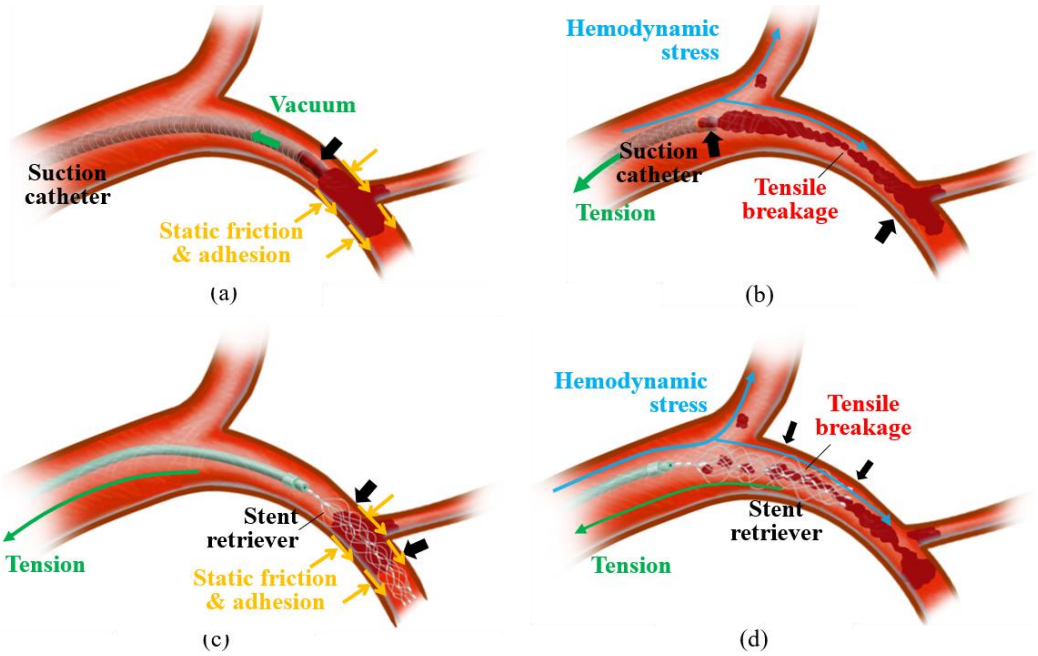

Figure 2.8 Forces involved in the clot removal with the suction catheter and stent retriever: (a) the suction catheter engages the clot by vacuum (black arrow), (b) withdrawal of the catheter exerts linear tension forces at the clot between the engagement segment and the clot/vascular surface interface (black arrows) and causes the clot to elongate, fracture and releases fragments that embolize downstream by blood flow (blue arrows), (c) the stent retriever applies tension at the region of stent/clot integration (black arrows) which generally overlaps with the place of maximal resistance forces, and (d) maintained tension leads to clot elongation, weakening and multifocal fragmentation with decrease of clot integration (black arrows) concurrent to increased hemodynamic stress due to restored blood flow.

Our analysis showed that emboli loaded with tensile forces elongated from 105% to 490% and developed single or multiple fractures leading to fragmentation. Clinically, these findings are relevant because both suction catheters and stent retrievers are based on the classical paradigm of *en bloc* removal of embolus by generating tensile forces (Figures 2.5 and 2.8). The tensile forces must overcome the resistance forces (including the static friction, adhesion of embolus to vascular surface, pressure gradient across the embolus, and clot reactive force) by applying a load, and in this process the clot elongates, weakens and is reduced in diameter which leads to possible fracture. If the thrombectomy device can load the clot with enough force and if the clot can withstand, the clot will become disimpacted, start to move and the removal process will begin. At this stage, emboligenic forces includes the kinetic friction of the clot against the vascular surface and the hemodynamic forces related to the blood flow. After the clot is moved,

required tensile forces to overcome emboligenic forces are lower given reduction of the resistance forces, but given clot elongation, weakening and fragmentation resulting for axial load, iatrogenic embolization is at risk of occurring. This phenomenon is enhanced by the reduction of clot diameter related to elongation with at least partial luminal reconstitution, that leads to flow through the previously stagnant arterial segment, which in turn favors downstream showering of the clot fragments. In this study, 62% (10 out of 16) of the patient clots were associated with inhomogeneous elongation with multifocal thinning and weakening likely leading to a highly emboligenic situation in the presence of arterial flow.

In addition, we have demonstrated that clots from patients are generally highly heterogeneous both histologically and mechanically, and therefore may elongate and fracture at different stresses during thrombectomy. The patient clots were composed of 0.45% to 91% (43%±35%) RBC, 0 to 95% (40%±37%) fibrin, and 1.7% to 56% (18%±16%) platelets, which is aligned with the values found in the literature [20,23–25]. Likewise, ultimate tensile strength varied greatly, with clot fractures occurring at ultimate strains from 1.05 to 4.89 (2.41±1.04) and ultimate stress from 63 to 2,396 kPa (569±695 kPa). These results reflect the highly heterogeneous and varied compositions of patient clots, both among patients and within the same patient (possibly related to different clot ages) and support a strong and significant ($p < 0.05$) dependence of ultimate tensile strength on clot composition. These factors, along with higher resistance forces due to prolonged clot/endothelial interaction in patients, suggest that fragmentation and iatrogenic embolization may be significantly more common than that observed in the testbed and likely underdiagnosed in clinical practice.

Another finding of our study is that under tension, the patient clots became stiffer as the strain increased, showing a strain-hardening property. As shown in the stress-strain curves, clot stress increases with strain and increases faster as the strain becomes larger. A similar phenomenon has been found in tensile tests of EAs,[26,27] and may be due to two reasons: 1) as the clot elongates, the weaker part of the clot fractures, leaving the stronger fibrin network behind to elongate and 2) the individual fibrin fibers are material with strain-hardening effect.[29] In addition, we have demonstrated that clots with a higher fibrin percentage have higher ultimate tensile stress and are therefore more difficult to break by linear pulling from the suction catheter or the stent retriever. The effect of fibrin on clot mechanics is clinically relevant and suggests that during mechanical thrombectomy the elongating clots will undergo increase in stiffness

leading to even stronger pull and higher risk of endothelial avulsion and vascular damage, or fracture leading to partial embolus removal and potentially free-floating fragments. This is especially relevant with greater clot length as a larger surface area between the clot and the vessel would yield to higher resistance forces. In addition, a recent publication suggest that fibrin-rich clots have a significantly higher coefficient of friction than clots with a RBC percentage >20% [12], and therefore may lead to higher resistance force to overcome.

Based on the findings of this study, technologies capable of challenging the classical parading of *en bloc* removal by safely fragmenting clots in-situ but extravascularly for piecemeal removal with a "single-pass" could be biomechanically superior to the suction catheters and stent retrievers for at least three reasons. First, the total resistance forces of the clot to the vessel wall would be dramatically reduced to the clot area actively undergoing maceration. In turn, this would lead into lower removal forces needed to efficiently remove the clot and reduce the likelihood of endothelial damage. Second, clot fragmentation would prevent clogging of the suction catheter; therefore, preventing loss of suction forces. Third, limiting uncontrolled intravascular elongation and fracture of clots could reduce free-floating fragments and embolization. A technology with these characteristics could greatly improve our ability to completely recanalize large vessel occlusions with minimal embolization and is to date an unmet clinical need. A device implementing these characteristics has been developed in this thesis work and will be covered in Chapters 4 and 5.

Several limitations are acknowledged in this study. First, the testbed does not mimic the biological interaction of the endothelium to the clots. We speculate that for stroke patients, the resistance forces are significantly stronger than that generated in our testbed which would lead to higher tensile forces needed to remove the clots. Second, clots analyzed in this study could be biased due to three facts: 1) only the 75 clots which were successfully retrieved during mechanical thrombectomy were analyzed , 2) only the 37 clots were big enough to be tensile tested , and 3) 21 clots were discarded due to clots slipping of the hemostats or concentrated stress at the hemostats. Notwithstanding these limitations, we believe that this fundamental mechanistic analysis expands our understanding of the complex clot-device interaction, provides biomechanical explanations for failure modes of current mechanical thrombectomy devices, and lay the groundwork to generate CAs with representative mechanical strength and histological composition to improve preclinical development and evaluation of thrombectomy devices.

2.5 Conclusions

Current thrombectomy devices remove clots mostly by applying linear tensile forces. Clots elongate until dissociation, which is preceded by focal thinning, multifocal fracture, cavitated fracture or stress concentrated fracture. Clot strength is highly variable and significantly correlates with the clot composition, which varies across different clots and within the same clot. The dynamic intravascular weakening of clots during removal with current devices under physiological flow conditions leads to a stage prone for iatrogenic embolization and the need of multiple attempts to completely recanalize arteries. The tensile properties and histology study for the clots from LVO stroke patients can also serve as a guide to fabricate realistic CAs for mechanical thrombectomy studies.

2.6 References

[1] Palaniswami M, Yan B (2015) Mechanical thrombectomy is now the gold standard for acute ischemic stroke: implications for routine clinical practice. *Interventional Neurology* 4(1–2):18–29.

[2] Chartrain AG, Awad AJ, Mascitelli JR, Shoirah H, Oxley TJ, Feng R et al. (2017) Novel and emerging technologies for endovascular thrombectomy. *Neurosurgical Focus* 42(4):E12.

[3] Zaidat OO, Yoo AJ, Khatri P, Tomsick TA, Von Kummer R, Saver JL et al. (2013) Recommendations on angiographic revascularization grading standards for acute ischemic stroke: A consensus statement. *Stroke* 44(9):2650–2663.

[4] Kleine JF, Wunderlich S, Zimmer C, Kaesmacher J (2017) Time to redefine success? TICI 3 versus TICI 2b recanalization in middle cerebral artery occlusion treated with thrombectomy. *Journal of NeuroInterventional Surgery* 9(2):117–121.

[5] Klinger-gratz PP, Schroth G, Gralla J, Jung S, Weisstanner C, Verma RK et al. (2015) Protected stent retriever thrombectomy prevents iatrogenic emboli in new vascular territories. *Neuroradiology* 571045–1054.

[6] Kurre W, Vorlaender K, Aguilar-Pérez M, Schmid E, Bäzner H, Henkes H (2013) Frequency and Relevance of Anterior Cerebral Artery Embolism Caused by Mechanical Thrombectomy of Middle Cerebral Artery Occlusion. *AJNR American Journal of Neuroradiology* 34(8):1606–1611.

[7] Saver JL (2006) Time Is Brain — Quantified. *Stroke* 37(1):263–266.

[8] Yoo AJ (2017) Thrombectomy in Acute Ischemic Stroke: Challenges to Procedural Success. *Journal of Stroke* 19(2):121–130.

[9] Teng D, Pannell JS, Rennert RC, Li J, Li Y, Wong VW et al. (2015) Endothelial Trauma From Mechanical Thrombectomy in Acute Stroke: In Vitro Live-Cell Platform With Animal Validation. *Stroke* 46(4):1099–1106.

[10] Reddy A, Liu Y, Gebrezgiabhier D, Davis E, Cockrum J, Zheng Y et al. Construction of Test-Bed for Research in Mechanical Thrombectomy in Stroke. *Journal of NeuroInterventional Surgery* (submitted).

[11] Duffy S, Farrell M, Mcardle K, Thornton J, Vale D, Rainsford E et al. (2017) Novel methodology to replicate clot analogs with diverse composition in acute ischemic stroke. *Journal of Neurointerventional Surgery* 9(5):486–491.

[12] Gunning GM, Mcardle K, Mirza M, Duffy S, Gilvarry M, Brouwer PA (2018) Clot friction variation with fibrin content; implications for resistance to thrombectomy. *Journal of NeuroInterventional Surgery* 10(1):34–38.

[13] Turk AS, Spiotta A, Frei D, Mocco J, Baxter B, Fiorella D et al. (2014) Initial clinical experience with the ADAPT technique: A direct aspiration first pass technique for stroke thrombectomy. *Journal of Neurointerventional Surgery* 6231–237.

[14] Blanc R, Redjem H, Ciccio G, Smajda S, Desilles JP, Orng E et al. (2017) Predictors of the Aspiration Component Success of a Direct Aspiration First Pass Technique (ADAPT) for the Endovascular Treatment of Stroke Reperfusion Strategy in Anterior Circulation Acute Stroke. *Stroke* 48(6):1588–1593.

[15] Schindelin J, Arganda-Carreras I, Frise E, Kaynig V, Longair M, Pietzsch T et al. (2012) Fiji: an open-source platform for biological-image analysis. *Nature Methods* 9(7):676–82.

[16] Mctaggart RA, Tung EL, Yaghi S, Cutting SM, Hemendinger M, Gale HI et al. (2017) Continuous aspiration prior to intracranial vascular embolectomy (CAPTIVE): a technique which improves outcomes. *Journal of Neurointerventional Surgery* 91154–

1159.

[17] Sporns PB, Hanning U, Schwindt W, Velasco A, Minnerup J, Zoubi T et al. (2017) Ischemic Stroke: What Does the Histological Composition Tell Us about the Origin of the Thrombus? *Stroke* 48(8):2206–2210.

[18] Li X, Lewis MT, Huang J, Gutierrez C, Osborne CK, Wu M-F et al. (2008) Intrinsic Resistance of Tumorigenic Breast Cancer Cells to Chemotherapy. *Journal of the National Cancer Institute* 100(9):672–679.

[19] Marder VJ, Chute DJ, Starkman S, Abolian AM, Kidwell C, Liebeskind D et al. (2006) Analysis of Thrombi Retrieved From Cerebral Arteries of Patients With Acute Ischemic Stroke. *Stroke* 37(8):2086–2093.

[20] Kim SK, Yoon W, Kim TS, Kim HS, Heo TW, Park MS (2015) Histologic analysis of retrieved clots in acute ischemic stroke: Correlation with stroke etiology and gradient-echo MRI. *AJNR American Journal of Neuroradiology* 36(9):1756–1762.

[21] Kan I, Yuki I, Murayama Y, Viñuela FA, Kim RH, Vinters HV et al. (2010) A novel method of thrombus preparation for use in a swine model for evaluation of thrombectomy devices. *AJNR American Journal of Neuroradiology* 31(9):1741–1743.

[22] Luo ZH, Chung A, Choi G, Lin YH, Uchida BT, Pavcnik D et al. (2012) Creation of Fibrinogen-enhanced Experimental Blood Clots to Evaluate Mechanical Thrombectomy Devices for Treatment of Acute Stroke : An In Vitro Study. *Laboratory Investigation* 23(8):1077–1083.

[23] Niesten JM, Van Der Schaaf IC, Van Dam L, Vink A, Vos JA, Schonewille WJ et al. (2014) Histopathologic composition of cerebral thrombi of acute stroke patients is correlated with stroke subtype and thrombus attenuation. *PLoS ONE* 9(2):12–14.

[24] Liebeskind DS, Sanossian N, Yong WH, Tsang MP, Moya AL, Zheng DD et al. (2011) CT and MRI early vessel signs reflect clot composition in acute stroke. *Stroke* 42(5):1237–1243.

[25] Boeckh-Behrens T, Schubert M, Förschler A, Prothmann S, Kreiser K, Zimmer C et al. (2016) The impact of histological clot composition in embolic stroke. *Clinical Neuroradiology* 26(2):189–197.

[26] Dempfle C-E, Kälsch T, Elmas E, Suvajac N, Lücke T, Münch E et al. (2008) Impact of fibrinogen concentration in severely ill patients on mechanical properties of whole blood

clots. *Blood Coagulation & Fibrinolysis : An International Journal in Haemostasis and Thrombosis* 19(8):765–770.

[27] Chueh JY, Wakhloo AK, Hendricks GH, Silva CF, Weaver JP, Gounis MJ (2011) Mechanical characterization of thromboemboli in acute ischemic stroke and laboratory embolus analogs. *AJNR. American Journal of Neuroradiology* 32(7):1237–1244.

[28] Kim OV., Litvinov RI, Weisel JW, Alber MS (2014) Structural basis for the nonlinear mechanics of fibrin networks under compression. *Biomaterials* 35(25):6739–6749.

[29] van Kempen THS, Peters GWM, van de Vosse FN (2015) A constitutive model for the time-dependent, nonlinear stress response of fibrin networks. *Biomechanics and Modeling in Mechanobiology* 14(5):995–1006.

[30] van Kempen THS, Donders WP, van de Vosse FN, Peters GWM (2016) A constitutive model for developing blood clots with various compositions and their nonlinear viscoelastic behavior. *Biomechanics and Modeling in Mechanobiology* 15(2):279–291.

[31] Merritt W, Holter AM, Beahm S, Gonzalez C, Becker TA, Tabor A et al. (2018) Quantifying the mechanical and histological properties of thrombus analog made from human blood for the creation of synthetic thrombus for thrombectomy device testing. *Journal of NeuroInterventional Surgery* 10(12):1168–1173.

[32] Huang CC, Chen PY, Shih CC (2013) Estimating the viscoelastic modulus of a thrombus using an ultrasonic shear-wave approach. *Medical Physics* 40(4):042901.

[33] Krasokha N, Theisen W, Reese S, Mordasini P, Brekenfeld C, Gralla J, et al. (2010) Mechanical properties of blood clots - A new test method. *Materialwissenschaft Und Werkstofftechnik* 41(12):1019–1024.

[34] Malone F, McCarthy E, Delassus P, Fahy P, Kennedy J, Fagan AJ et al. (2018) The mechanical characterisation of bovine embolus analogues under various loading conditions. *Cardiovascular Engineering and Technology* 9(3):489–502.

CHAPTER 3
FABRICATION, HISTOLOGY AND TENSILE PROPERTIES OF HUMAN BLOOD CLOT ANALOGS

3.1 Introduction

The low success rate for complete clot removal using current thrombectomy devices reflects a lack of knowledge of the interaction between clots and mechanical thrombectomy devices, such as the suction catheter and stent retriever. The limited access to patient clots leads to the need for realistic CAs with similar mechanical properties as patient clots. To study the clot-device interaction and improve patient outcome, CAs are necessary for mechanical thrombectomy devices testing.

Most studies used animal blood , such as porcine [1–6] and bovine [6,7] whole blood, to make CAs, due to the limited access to human blood. For the studies with human blood material, whole blood [5,6,8] or pure plasma [9] were used. Those CAs have very limited variance in terms of composition and therefore can't well represent the patient clots which are highly variant in the composition, as have been shown in Chapter 2. CAs with variant compositions were made by mixing RBC, plasma, and platelets with different volume ratios but the ovine blood materials were used and the mechanical properties of the CAs were not characterized [10]. The research gap is to make CAs from human blood material with variant compositions. In this chapter, RBC, plasma, and platelets from human blood were mixed with different volume ratios to produce a range of CAs.

The clot tensile strength is an important factor affecting the clot-device interaction. As shown in Chapter 2, during the clot removal using the suction catheter or stent retriever, clots are pulled and under a significant tensile deformation. The tensile strength of the clot affects the

fragmentation of clots, which is common in mechanical thrombectomy. For the suction catheter, a clot can clog the catheter if the clot is not fragmented by the vacuum inside the catheter. For the stent retriever, the stent expands into and engages with the clot for pulling. While pulling, the clot is under tension and may break. The clot fragments may flow into tributaries and cause distal embolization [11]. It is important to study the tensile strength of clot to understand the clot fragmentation for improvement of the efficacy and safety of mechanical thrombectomy procedure.

The tensile strength of CAs with different compositions has not been widely studied. The uniaxial tensile test has been used to quantify the stiffness and mechanical strength of CAs made from human and porcine whole blood [12] and bovine whole blood [7]. Such CAs made from whole blood were intrinsically limited in the composition variety. The patient clots, however, are known to have a large range of RBC, fibrin, and platelet percentages as shown in Chapter 2 and in the literature [13–16].

The goal of this study is to fabricate CAs that can mimic the patient clots in compositions and tensile properties for the mechanical thrombectomy devices' testing. The aims are: 1) to fabricate human CAs with a wide range of RBC, fibrin, and platelet composition similar to patient clots, and 2) to evaluate the tensile properties and compare to results of patient clots. CAs were fabricated by mixing various volume ratios of RBC, plasma, and platelets, and molded to the dogbone-shaped tensile specimen. Percentages of RBC, fibrin and platelets of CA specimens were quantified in histology. The tensile test of CA specimens was conducted. The tensile force, displacement, and cross-section area during test were measured. The stiffness and strain and strength at failure were measured using the uniaxial tensile test and compared to patient clots' tensile test data in Chapter 2. The relationships between the volume ratio of the blood materials and CA composition, as well as the clot composition and tensile properties were analyzed.

3.2 Materials and Methods

3.2.1 Clot Analog Fabrication

Dogbone-shaped CAs were molded with different ratios of RBC, plasma, and platelets acquired from the University of Michigan Blood Bank. The RBC, plasma and platelets were measured by volume (typically 40 mL in total for one batch) and then mixed using a magnetic mixer (Model SP88857100; Thermo Scientific, Waltham, MA) for two minutes at 300 rpm. Calcium chloride solution (0.2% concentration) was slowly added to the mixture to reverse the citrate phosphate dextrose (CPD) and induce coagulation [10,17]. The mixture was injected into the mold, as shown in Figure 3.1, to mold the dogbone-shaped CA tensile specimens. Dimensions of the specimen with circular cross-section for a uniform stress distribution were adopted from the geometry based on ASTM D638-10 Type IV [18]. The mold was 3D-printed with 25 μm layer height using a stereolithography 3D-printer (Form 2; Formlabs, Somerville, Massachusetts). A clear coating (ColorMaster® Acrylic Spray Paint; Krylon Products Group, Cleveland, Ohio) was applied to the mold to smooth the surface of the mold and molded CA specimens. The mixture rested for 1.5 hours for coagulation before testing.

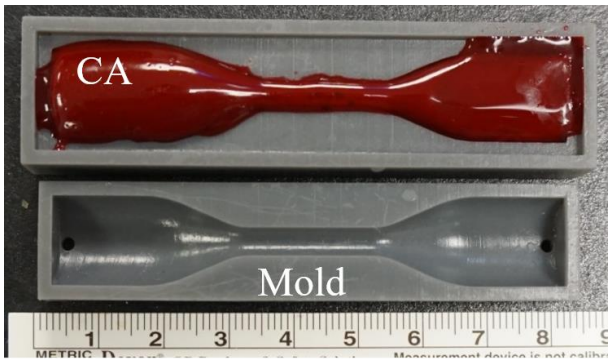

Figure 3.1 Forming the CA in the dogbone-shaped mold.

Ten types of CA specimens with varied volume ratios of RBC, plasma, and platelets were fabricated. The plasma volume ratio (i_F) has 4 levels (30%, 45%, 60%, and 80%) and platelet volume ratio (i_P) has 3 levels (20%, 30%, and 40%), with the rest being RBC volume ratio (i_R). Those percentage levels were decided with the aim to mimic the range of clot compositions

presented in Chapter 2 and in the literature [13–16]. The detailed ingredient for each of the ten types of CA specimens is shown in Table 3.1. Five CA specimens were made for each CA type. A total of 50 CAs were made and analyzed by tensile test. The final composition (RBC, fibrin, and platelets) in the CAs are different from the volume ratios and was analyzed by histology.

Table 3.1 CAs' ingredients with 10 different ratio combinations.

CA #	i_R (%)	i_F (%)	i_P (%)
1	50	30	20
2	40	30	30
3	30	30	40
4	35	45	20
5	25	45	30
6	15	45	40
7	20	60	20
8	10	60	30
9	0	60	40
10	0	80	20

3.2.2 Tensile Test Setup

The tensile test pulled the CA specimen until it breaks. The deformation and tensile force were measured. As shown in Figure 3.2(a), the CA specimen was gripped by two hemostats at the bulged ends. One hemostat was fixed to a linear stage (Model 200cri; Siskiyou, Grants Pass, Oregon) and was pulled at a slow and constant speed of 0.3 mm/s for quasi-static tensile deformation. The other hemostat was fixed to a stationary force transducer (Model Gamma; ATI Industrial Automation, Apex, North Carolina). The tensile force on the hemostat was measured at a sampling rate of 50 Hz. The data was processed using the moving average for every 5 data points. Figure 3.2(b) shows a sample tensile force vs. pulling distance for one of CA #7 specimens. The pulling force increases as the linear stage moves to pull the CA specimen and abruptly drops to zero when the CA specimen is fractured. A video camera (Model α6000; Sony, Tokyo, Japan) recorded digital images of the deformed CA specimen at 30 frames per second

from the top. Two fiducials, as marked in Figure 3.2(a), were marked on the CA specimen to define the gage zone before pulling. Locations of these two fiducials were measured to track the elongation of the CA specimen between the two fiducials during tensile test. An open-source image processing software, Kinovea (v0.8.15) was used to find the distance L between the two fiducials to calculate the elongation and engineering strain ε:

$$\varepsilon = \frac{L}{L_0} - 1 \tag{3.1}$$

where L_0 is the distance between the fiducials when the pulling force. The a small (2 mN) tensile force F is defined as the start of the tensile test. At fracture, the CA specimen has an ultimate strain of ε_{ut}.

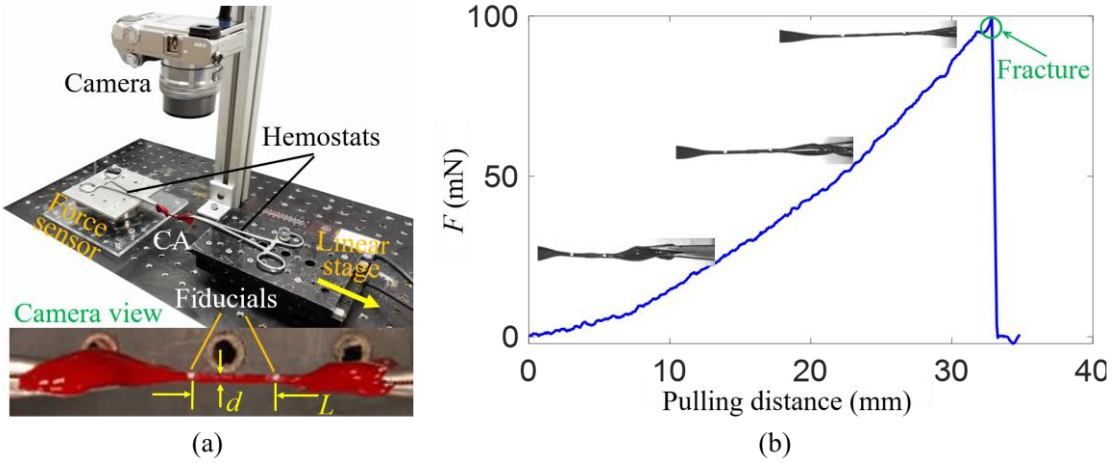

Figure 3.2 (a) Tensile test setup and (b) a sample pulling force measurement for CA #7.

The tensile force on the CA specimen was divided by the cross-sectional area of the specimen to calculate the stress. Assuming the cross-section of the CA specimen remain circular during tensile pulling, the diameter of the CA specimen, d, is measured using an edge detection algorithm implemented in Matlab (v2017b; MathWorks®, Natick, Massachusetts). The normalized loading on the CA, or true stress σ, is calculated as:

$$\sigma = \frac{4F}{\pi d^2} \tag{3.2}$$

At fracture, the CA specimen has an ultimate stress, σ_{ut}. To evaluate the stiffness of the CA specimen, i.e. the resistance of the CA specimen to elongation under pulling, the elastic modulus $E_{0\text{-}0.45}$ was calculated as:

$$E_{0-0.45} = \frac{\sigma_{0.45}}{0.45} \tag{3.3}$$

where $\sigma_{0.45}$ is the tensile stress on the specimen at a stain of 0.45. $E_{0\text{-}0.45}$ was also used to evaluate the CA stiffness for compression test [6].

3.2.3 Histology Assessment

After tensile testing, a sample of CA was cut off for histology analysis to find the histological percentages of RBC, fibrin, and platelets in following three steps. First, the CA sample was stained with H&E to show RBC in dark red [2,3,10,14,15,19–21] and CD61 to show platelets in dark brown [15]. Second, a microscope (Axioskop 2 plus; Zeiss, Oberkochen, Germany) was used at 400× and 600× magnifications to scan the H&E stained and CD61 stained slides, respectively. The images were captured by a digital camera (AxioCam MRc5; Zeiss, Oberkochen, Germany) at 2584×1936 resolution. Figures 3.3 show the microscopic images for all the 10 types of CAs with H&E and CD61 stain. The images show the fibrin network and platelet aggregates are mostly homogeneously distributed throughout the formed CAs.

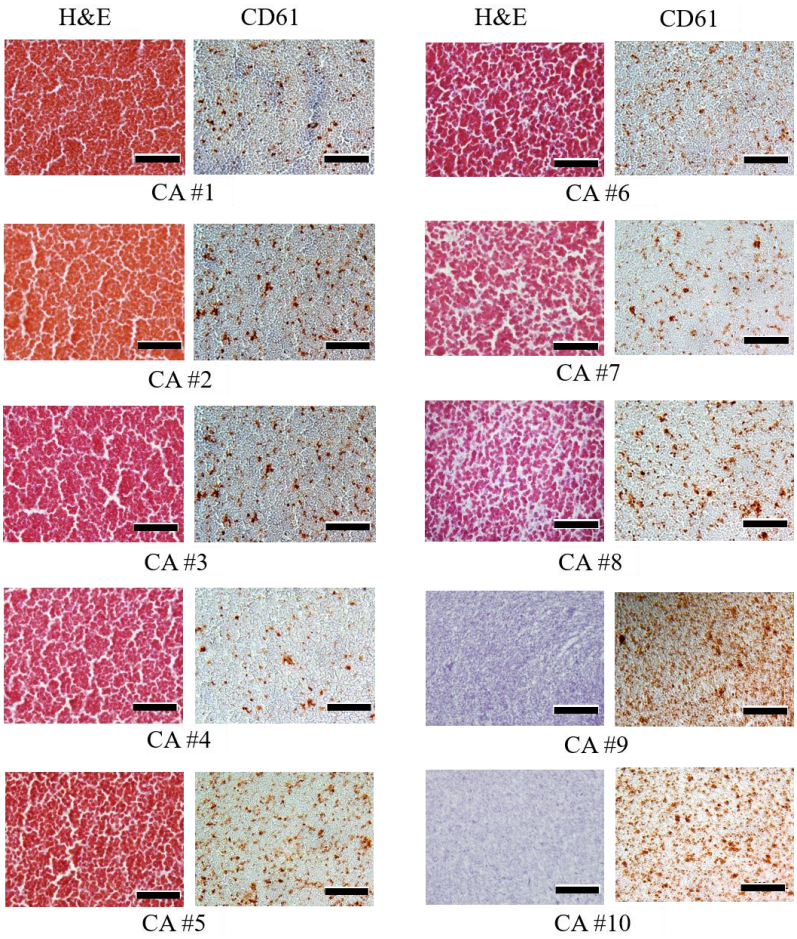

Figure 3.3 Images of H&E and CD61 stain for the 10 types of CA. Scale bar = 100 μm.

Finally, the microscopic images were processed using ImageJ (v1.52; National Institute of Health) to apply color masks to quantify the area percentages of RBC (h_R) and platelet (h_P) under the guide of a senior pathologist. The balance was assumed to be fibrin and has a percentage $h_F = 1 - h_R - h_P$.

3.2.4 Statistical Analysis

A multi-variable linear regression model was built to predict the histological percentages of RBC, fibrin, and platelets in the CAs based on the given volume ratios of RBC, plasma, and platelets. The histology results for all the CAs (n = 50) were used to fit the model and the goodness of fit was evaluated by calculating the coefficient of determination (R^2).

Pearson correlation coefficient was calculated and used to evaluate how the CA composition (histological percentages of RBC, fibrin, and platelet) affects the CA tensile

properties (elastic modulus and ultimate strain and stress). This statistical analysis was carried out using IBM SPSS Statistics (v24.0). $p < 0.05$ was considered statistically significant.

3.3 Results

3.3.1 Histological Composition of CA

Table 3.2 shows the percentages of the composition for the formed CAs with mean and one standard deviation and comparison with six patient clots from Chapter 2. Those six clots are selected because they have single focal fracture, the same fracture pattern as the CAs in this study. The CAs have 0 to 96% RBC, 0.78% to 92% plasma, and 2.1% to 22% platelets and is similar to that found in stroke patients in Chapter 2 and in the literature [13–16].

Table 3.2 Histology results for the CAs and comparison with patient clots.

	Clot	RBC (%)	Fibrin (%)	Platelets
Clot analog	1	95.9±2.3	2.1±2.3	2.1±0.4
	2	96.3±0.6	0.8±0.6	2.9±0.4
	3	79.9±1.9	16.0±1.6	4.1±0.6
	4	84.8±2.6	12.9±2.2	2.3±0.5
	5	84.6±3.0	12.9±2.2	2.3±0.5
	6	77.8±4.8	18±2.7	4.2±2.2
	7	75.6±5.6	21.8±6.6	2.6±1.5
	8	46.7±10.0	49.7±10.0	3.6±1.1
	9	0±0	77.8±12.5	22.2±12.5
	10	0±0	91.8±1.7	8.2±1.7
Patient clot	1	90.3	0	9.7
	2A	89.2	1.6	9.2
	3	90.7	2.3	7.0
	2B	79.0	16.8	4.2
	4	69.3	29.0	1.7
	2C	15.4	67.8	16.8

With the histology results, the multi-linear regression models to predict the histological percentages of RBC, fibrin, and platelets in the CAs are fitted and are as follows:

$$h_R = 2.030 i_R + 0.016 i_F + 0.612 i_P \tag{3.4}$$

$$h_F = -0.868 i_R + 0.937 i_F + 0.155 i_P \tag{3.5}$$

$$h_P = -0.161 i_R + 0.048 i_F + 0.234 i_P \tag{3.6}$$

The model-predicted percentages have errors of 13.7%, 11.3%, and 3.59% and R^2 values of 0.786, 0.804, and 0.341 for histological percentage of RBC, fibrin, and platelets, respectively. The low correlation for the platelet percentage might be due to two reasons: 1) the small range (20%-40%) of platelet volume ratios tested in this study, and 2) the aggregation of platelets. For all three equations, the fittings are very statistically significant with $p < 0.001$.

3.3.2 Tensile Test Results

Figure 3.4 shows the averaged stress-strain curves for all 10 types of CA specimen. For all the CAs, stress on the CA specimen increases with strain and increase faster as the strain becomes larger. CAs have a large range of $E_{0\text{-}0.45}$ from 11 to 114 kPa. CAs also have a large range of tensile strength, with ε_{ut} ranging from 0.78 to 1.36 and σ_{ut} ranging from 16 to 949 kPa (a variation of 59 times). This is related to the large variation of the CA composition, as shown in Table 3.2. CA #9 has the highest platelet percentage and the largest ε_{ut}. CA #10 has the highest fibrin percentage and the largest $E_{0\text{-}0.45}$ and σ_{ut}.

CAs in this study can mimic the tensile properties with some difference. As shown in Figure 3.4, the six dashed lines are the stress-strain curves of six patient clots under the uniaxial tensile test from Chapter 2 and show similar stress-strain curves compared to the CAs. Those six patient clots were selected since they have the single fracture pattern during the tensile test, representing a homogeneous composition compared to the other 10 patient clots. Among these six patient clots, the patient clot 2B (black dashed line) has a very similar stress-strain curve compared to CA #6 (yellow solid line). They also share a very similar histological composition, as shown in Table 3.2. Compared to 2B, CA #6 is about 6% higher in ε_{ut}, 20% lower in σ_{ut}, and 50% higher in $E_{0\text{-}0.45}$ (42 vs 28 kPa).

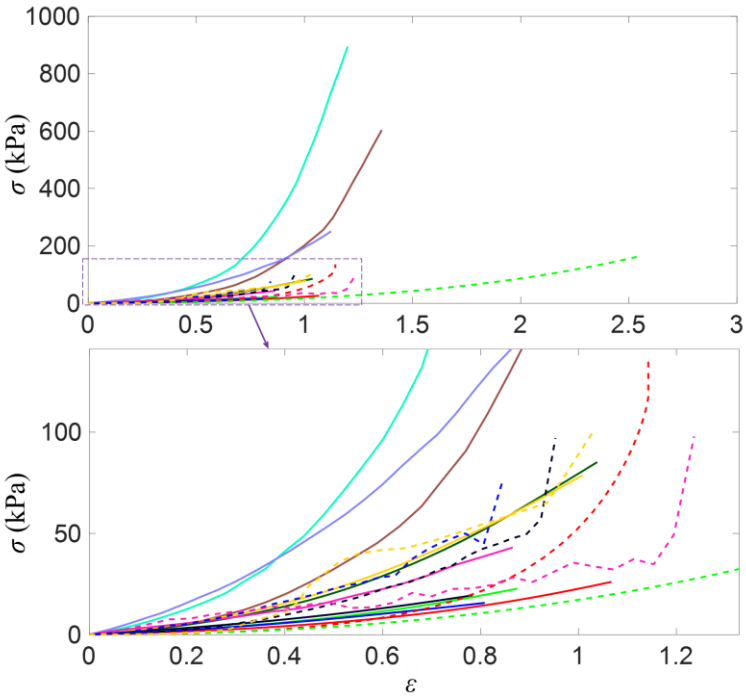

CA #	$E_{0\text{-}0.45}$ (kPa)	ε_{ut}	σ_{ut} (kPa)
1	13	0.81	16
2	11	1.07	28
3	16	0.88	22
4	19	0.78	20
5	31	0.87	41
6	42	1.01	77
7	38	1.04	91
8	106	1.12	292
9	57	1.36	446
10	114	1.20	949
1	43	0.84	76
2A	8	1.14	135
3	7	2.54	161
2B	27	0.95	97
4	33	1.24	98
2C	54	1.03	101

Figure 3.4 Tensile test results for the CAs and comparison with 6 patient clots.

3.3.3 Correlation between CA Tensile Properties and Composition

Table 3.3 shows the correlation result between the tensile properties ($E_{0\text{-}0.45}$, ε_{ut}, and σ_{ut}) and CA composition (h_R, h_F, and h_P) based on the analysis of 50 CA specimens. The elastic modulus ($E_{0\text{-}0.45}$) is strongly ($|r| \geq 0.6$) and negatively correlated with RBC percentage ($p < .001$), strongly and positively correlated with fibrin percentage ($p < .001$), and moderately ($0.3 < |r| \leq 0.6$) and positively correlated with platelet percentage ($p = 0.013$). The ultimate tensile strain (ε_{ut}) is moderately and negatively correlated with the RBC percentage ($p < .001$) and moderately and positively correlated with the fibrin percentage ($p < .001$). The ultimate tensile stress (σ_{ut}) is strongly and negatively correlated with the RBC percentage ($p < .001$), strongly and positively correlated with the fibrin percentage ($p < .001$), and moderately and positively correlated with the platelet percentages ($p = 0.004$).

Table 3.3 Correlation analysis results of the CA composition and CA tensile properties.

	h_R		h_F		h_P	
	r	*p*	*r*	*p*	*r*	*p*
$E_{0\text{-}0.45}$	–0.609	< .001***	0.613	< .001***	0.349	0.013*
ε_{ut}	–0.536	< .001***	0.555	< .001***	0.240	0.093
σ_{ut}	–0.696	< .001***	0.702	< .001***	0.395	0.004**

* $p < 0.05$; ** $p < 0.01$; *** $p < 0.001$

Table 3.4 shows the correlation result between the tensile properties ($E_{0\text{-}0.45}$, ε_{ut}, and σ_{ut}) and CA ingredient volume ratios (i_R, i_F, and i_P) based on the analysis of 50 CA specimens. The elastic modulus ($E_{0\text{-}0.45}$) is strongly and negatively correlated with RBC volume ratio ($p < .001$), and strongly and positively correlated with plasma volume ratio ($p < .001$). The ultimate tensile strain (ε_{ut}) is moderately and negatively correlated with the RBC volume ratio ($p < .001$), and moderately and positively correlated with the plasma volume ratio ($p = 0.004$). The ultimate tensile stress (σ_{ut}) is moderately and negatively correlated with the RBC volume ratio ($p < .001$), and strongly and positively correlated with the plasma volume ratio ($p < .001$). None of $E_{0\text{-}0.45}$, ε_{ut}, or σ_{ut} is significantly correlated with the platelet percentage, which could due to the poor correlation ($R^2 = 0.341$) between the platelets volume ratio and platelets percentage in the CAs.

Table 3.4 Correlation between the CA ingredient volume ratios and tensile properties.

	i_R		i_F		i_P	
	r	*p*	*r*	*p*	*r*	*p*
$E_{0\text{-}0.45}$	–0.633	< .001***	0.678	< .001***	-0.069	.633
ε_{ut}	–0.483	< .001***	0.396	0.004**	0.176	.222
σ_{ut}	–0.583	< .001***	0.647	< .001***	-0.108	.456

** $p < 0.01$; *** $p < 0.001$

3.4 Discussions

The tensile properties (stiffness and tensile strength) of CAs are correlated to the CA composition and mainly depend on the fibrin percentage (with the highest *r*-values). CAs with higher fibrin content are stiffer, have larger elongation, and higher ultimate tensile stress. Such correlations can be explained by the mechanical properties of individual fibers within the CA's fibrin network.

CAs with higher fibrin percentage are stiffer (with higher $E_{0\text{-}0.45}$) since fibrin fibers are very stiff. Collet et al. [22] found the elastic moduli of fibrin fiber is about 14.5 MPa and it's much higher than that of CAs, indicating the stiffness of the CAs is mainly attributed to the fibrin fibers. Also, CAs behave stiffer as the strain increase, showing a strong strain-hardening property and such phenomenon was also reported during tensile test of CAs in the literature [5,7]. This can be explained by the strain-hardening property of individual fibrin fibers [23].

CAs with higher fibrin percentage can elongate more (with higher ε_{ut}). Fibrin fibers are very stretchable material and can elongate to about three times of its original length [23]. Combining this large elongation with the high stiffness of the fibrin fibers, CAs with higher fibrin percentage therefore can withstand higher tensile stress (with higher σ_{ut}) before fracture.

The difference of the tensile properties is much bigger when comparing the CAs in this study to all the patient clots in the literature. CAs in this study have ε_{ut} ranging from 0.78 to 1.36 and σ_{ut} ranging from 16 to 949 kPa, having much smaller upper bounds compared to those of patient clots (ε_{ut} ranging from1.05 to 4.89 and σ_{ut} ranging from 63 to 2,396 kPa).

The authors attribute such difference to two limitations of this study. First, CAs in this study are generally homogeneous, as shown in Figures 3.3(a)-(e), while patient clots are known to be quite inhomogeneous. For an inhomogeneous patient clot under pulling, weaker and less stiff part of the clot will be peeled off first and detach from the main clot block, leaving the stronger and stiffer part behind to elongate. This causes the clot to withstand larger elongation, as supported by the much larger ε_{ut} (up to 4.89) associated with multi-focal fracture compared to that with single focal fracture in Chapter 2. Second, CAs in this study did not subject to pulsatile pressure like the clot inside the blood vessel before testing, while clots for the stroke patients treated with mechanical thrombectomy can be 24 hours old [24]. Aging of a clot is a dynamics bio-chemical process and made the CA have stiffer compression response [25]. The mechanical

load on the clot due to the physiologically pulsatile flow within the human body can also change the fibrin network density [9].

3.5 Conclusions

This study proposed a fabrication method for CAs that could mimic the histological composition and tensile properties of clots extracted from stroke patients. The histological compositions could be predicted by a multi-linear regression model. The tensile properties (elastic modulus, ultimate tensile strain and ultimate tensile stress) were characterized by uniaxial tensile test and found to be significantly correlated to the clot composition. The CAs in this study can serve as a useful tool to facilitate the development of mechanical thrombectomy devices and valuable for other clot-related research.

3.5 References

[1] Gralla J, Schroth G, Remonda L, Fleischmann A, Fandino J, Slotboom J et al. (2006) A dedicated animal model for mechanical thrombectomy in acute stroke. *AJNR American Journal of Neuroradiology* 27(6):1357–61.

[2] Kan I, Yuki I, Murayama Y, Viñuela FA, Kim RH, Vinters HV et al. (2010) A novel method of thrombus preparation for use in a swine model for evaluation of thrombectomy devices. *AJNR. American Journal of Neuroradiology* 31(9):1741–1743.

[3] Luo ZH, Chung A, Choi G, Lin YH, Uchida BT, Pavcnik D et al. (2012) Creation of Fibrinogen-enhanced Experimental Blood Clots to Evaluate Mechanical Thrombectomy Devices for Treatment of Acute Stroke : An In Vitro Study. *Laboratory Investigation* 23(8):1077–1083.

[4] Shao Q, Zhu L, Li T, Li L, Li D, Zhang J et al. (2014) New method of thrombus preparation using a fl uid model for evaluation of thrombectomy devices in a swine model. *Thrombosis Research Journal* 1341087–1092.

[5] Krasokha N, Theisen W, Reese S, Mordasini P, Brekenfeld C, Gralla J et al. (2010) Mechanical properties of blood clots - A new test method. *Materialwissenschaft Und Werkstofftechnik* 41(12):1019–1024.

[6] Chueh JY, Wakhloo AK, Hendricks GH, Silva CF, Weaver JP, Gounis MJ (2011) Mechanical characterization of thromboemboli in acute ischemic stroke and laboratory embolus analogs. *AJNR American Journal of Neuroradiology* 32(7):1237–1244.

[7] Malone F, McCarthy E, Delassus P, Fahy P, Kennedy J, Fagan AJ et al. (2018) The mechanical characterisation of bovine embolus analogues under various loading conditions. *Cardiovascular Engineering and Technology* 9(3):489–502.

[8] Merritt W, Holter AM, Beahm S, Gonzalez C, Becker TA, Tabor A et al. (2018) Quantifying the mechanical and histological properties of thrombus analog made from human blood for the creation of synthetic thrombus for thrombectomy device testing. *Journal of NeuroInterventional Surgery* 10(12):1168–1173.

[9] Kim OV., Litvinov RI, Weisel JW, Alber MS (2014) Structural basis for the nonlinear mechanics of fibrin networks under compression. *Biomaterials* 35(25):6739–6749.

[10] Duffy S, Farrell M, Mcardle K, Thornton J, Vale D, Rainsford E et al. (2017) Novel methodology to replicate clot analogs with diverse composition in acute ischemic stroke. *Journal of NeuroInterventional Surgery* 9(5):486–491.

[11] Kurre W, Vorlaender K, Aguilar-Pérez M, Schmid E, Bäzner H, Henkes H (2013) Frequency and Relevance of Anterior Cerebral Artery Embolism Caused by Mechanical Thrombectomy of Middle Cerebral Artery Occlusion. *AJNR American Journal of Neuroradiology* 34(8):1606–1611.

[12] Monstadt H, Krasokha N, Dorn F, Reese S, Theisen W, Mordasini P et al. (2009) Mechanical properties of blood clots - A new test method. in: World Congr. Med. Phys. Biomed. Eng., Springer Berlin Heidelberg, Munich, Germanypp. 560–563.

[13] Liebeskind DS, Sanossian N, Yong WH, Tsang MP, Moya AL, Zheng DD et al. (2011) CT and MRI early vessel signs reflect clot composition in acute stroke. *Stroke* 42(5):1237–1243.

[14] Niesten JM, Van Der Schaaf IC, Van Dam L, Vink A, Vos JA, Schonewille WJ et al. (2014) Histopathologic composition of cerebral thrombi of acute stroke patients is correlated with stroke subtype and thrombus attenuation. *PLoS ONE* 9(2):12–14.

[15] Kim SK, Yoon W, Kim TS, Kim HS, Heo TW, Park MS (2015) Histologic analysis of retrieved clots in acute ischemic stroke: Correlation with stroke etiology and gradient-echo MRI. *AJNR American Journal of Neuroradiology* 36(9):1756–1762.

[16] Boeckh-Behrens T, Schubert M, Förschler A, Prothmann S, Kreiser K, Zimmer C et al. (2016) The impact of histological clot composition in embolic stroke. *Clinical Neuroradiology* 26(2):189–197.

[17] Gunning GM, Mcardle K, Mirza M, Duffy S, Gilvarry M, Brouwer PA (2018) Clot friction variation with fibrin content; implications for resistance to thrombectomy. *Journal of NeuroInterventional Surgery* 10(1):34–38.

[18] ASTM Committee D20 on Plastics (2010) Standard Test Method for Tensile Properties of Plastics. *ASTM International*.

[19] Sporns PB, Hanning U, Schwindt W, Velasco A, Minnerup J, Zoubi T et al. (2017) Ischemic Stroke: What Does the Histological Composition Tell Us about the Origin of the Thrombus? *Stroke* 48(8):2206–2210.

[20] Li X, Lewis MT, Huang J, Gutierrez C, Osborne CK, Wu MF et al. (2008) Intrinsic Resistance of Tumorigenic Breast Cancer Cells to Chemotherapy. *Journal of the National Cancer Institute* 100(9):672–679.

[21] Marder VJ, Chute DJ, Starkman S, Abolian AM, Kidwell C, Liebeskind D et al. (2006) Analysis of Thrombi Retrieved From Cerebral Arteries of Patients With Acute Ischemic Stroke. *Stroke* 37(8):2086–2093.

[22] Collet JP, Shuman H, Ledger RE, Lee S, Weisel JW (2005) The Elasticity of an Individual Fibrin Fiber in a Clot. *Proceedings of the National Academy of Sciences of the United States of America* 102(26):9133–9137.

[23] Liu W, Carlisle C, Sparks E, Guthold M (2010) The mechanical properties of single fibrin fibers. *Journal of Thrombosis and Haemostasis* 81030–1036.

[24] Nogueira RG, Jadhav AP, Haussen DC, Bonafe A, Budzik RF, Bhuva P et al. (2018) Thrombectomy 6 to 24 Hours after Stroke with a Mismatch between Deficit and Infarct. *New England Journal of Medicine* 378(1):11–21.

[25] Xie H, Kim K, Aglyamov SR, Emelianov SY, O'Donnell M, Weitzel WF et al. (2005) Correspondence of ultrasound elasticity imaging to direct mechanical measurement in aging DVT in rats. *Ultrasound in Medicine and Biology* 31(10):1351–1359.

CHAPTER 4
CUTTING OF BLOOD CLOTS – EXPERIMENT AND SMOOTH PARTICLE GALERKIN MODELLING

4.1 Introduction

A mechanical thrombectomy device using a high-speed rotating cutting tool at the tip inside the vacuum suction catheter to enhance clot removal, as shown in Figure 4.1(b), was proposed in 1997 [1]. The clot is deformed and drawn by vacuum into the catheter tip. The cutting tool, connected via a flexible drive shaft to a motor, rotates at 60,000 to 120,000 rpm and cuts the clot into chips. The chips are removed by vacuum suction. The goal of this study is to understand the clot cutting mechanics in this environment.

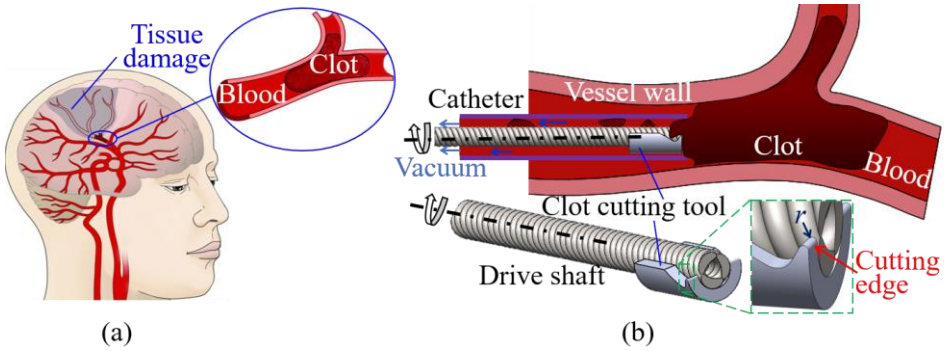

Figure 4.1 (a) Stroke caused by the clots and (b) cutting based clot removal.

The cutting force in oblique cutting of soft tissue using a sharp blade has been studied [2–4] and showed that the configuration with high rake and inclination angles has low cutting force and more effective cutting. The straight cutting edge in Figure 4.1(b) has varying inclination

angle along the cutting edge. Grinding of the clot cutting tool is studied to manufacture specified rake and inclination angles for clot cutting.

The tool tip cutting edge radius affects the clot cutting in the vacuum suction setup shown Figure 4.1(b). We have observed experimentally that a sharper cutting edge had resulted in a larger depth of cut, which led to difficulties in chip evacuation and the shaft breakage due to the accumulation of continuous chip. In this study, the cutting edge is manually honed to an edge radius (marked as *r* in Figure 4.1(b)) to balance the material removal rate and cutting force. If *r* is too large, the tool will not cut and remove the clot. If *r* is too small, the drive shaft can cut deep into the clot and create large clot chips. These large clot chips are difficult to be evacuated by the vacuum and will adhere to the drive shaft, increasing the friction and torque load on the drive shaft and may eventually break the drive shaft.

The clot cutting force is modelled using the smooth particle Galerkin (SPG) method. SPG is a mesh-free method with discrete particles to model the workpiece to avoid mesh entanglement in finite element modelling (FEM) [5,6]. A commonly used mesh-free method is the smooth particle hydrodynamics (SPH) method and was applied to predict the debris size [7] and force [8] in grinding of calcified plaque surrogate. However, SPH suffers from numerical defects such as tensile instability where the particles form small clumps due to the reduced attractive force between two particles when the material is under tension [9,10]. Such defects are solved in SPG by using strain regularization and updated Lagrangian kernel function as the workpiece deforms [11]. To the authors' knowledge, this study is the first to utilize SPG for machining modelling.

Experimental setups for clot cutting and cutting tool grinding are first introduced. SPG modelling of the clot cutting is then presented. Experimental measurements and SPG modelling results of the thrust and cutting forces are compared.

4.2 Experimental Setup for Clot Cutting Force Measurement

The clot cutting experimental setup, the clot cutting tool grinding, the clot cutting force measurement, and the clot workpiece fabrication are presented in this section.

4.2.1 Clot Cutting Experimental Setup

Figure 4.2 shows the experiment setup for clot cutting force measurement. The motor drive unit consisted of a brushless DC motor (Model ECXSP16L; Maxon Motor, Sachseln, Switzerland) with a speed up to 70,000 rpm and a spur gear set 4:1 gear ratio to increase the rotational speed by three times. The motor was powered by a DC power supply and controlled by a controller (Model ESCON 70/10; Maxon Motor, Sachseln, Switzerland) and had an encoder to achieve less than 0.5% of speed error. The motor current drawn was monitored to calculate the cutting force.

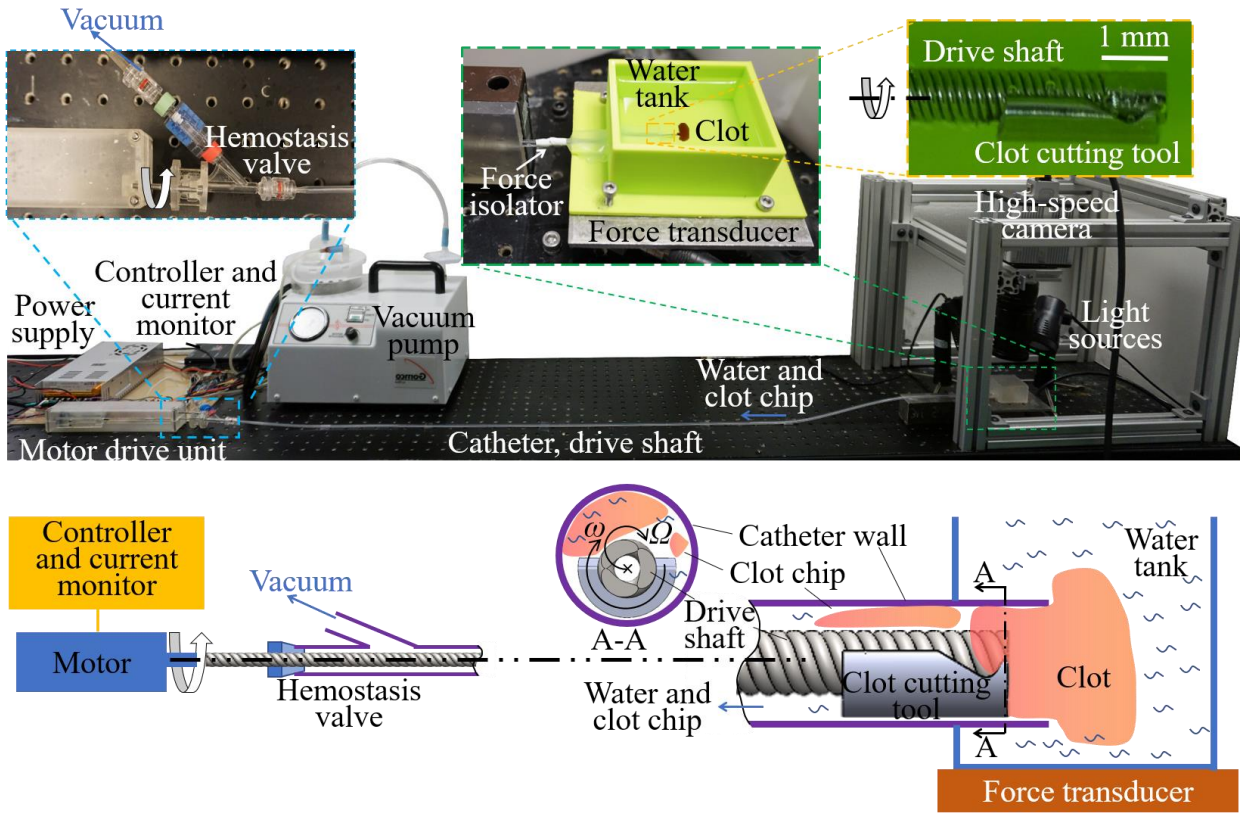

Figure 4.2 Experimental setup for clot cutting.

The electric motor rotated the drive shaft within the catheter. The drive shaft was made of four 0.13 mm diameter AISI 304 stainless wires wound together to form a flexible hollow shaft with 0.51 mm inner and 0.76 mm outer diameter. Similar shafts were used in devices for grinding the calcified plaque in the artery [12]. One end of the drive shaft was connected to the

motor and the other end was connected to the clot cutting tool. The catheter was a 1.32 m long clear perfluoroalkoxy (PFA) tube with 1.59 mm inner and 3.18 mm outer diameter.

A hemostasis valve (Model FLO50; Merit Medical, South Jordan, Utah) was used to separate the mixture of clot chips and water from the drive shaft using the Y-connector with a ring seal on one end and the vacuum pump on the other end. The vacuum was generated using a rotary vane pump (Model 01-12-405; Allied Healthcare, St. Louis, MO) to generate a 70 kPa vacuum at the tip of the catheter.

The tip of the catheter was placed inside a water tank with the clot workpiece at the front. A high-speed camera (Model FASTCAM-1024PCI; Photron, San Diego, CA) and light-source were used to acquire images of the clot cutting processes. A force transducer (Model Gamma; ATI Industrial Automation, Apex, North Carolina) was placed under the water tank to measure the thrust force in clot cutting. Near the water tank, the catheter was separated into two segments, which were connected via a flexible tube, serving as a force isolator to reduce shaft vibration transmitting to the clot cutting site.

4.2.2 Miniature Clot Cutting Tool

The clot cutting tool was manufactured by grinding an 18-gauge hard tempered AISI 316 stainless steel tube as shown in Figure 4.3(a). The spindle was attached to two linear stages (Model 200cri; Siskiyou, Grants Pass, Oregon). The steel tube was clamped using a 5C collet attached on a tilting table to tilt an angle θ between the tube axis and the spindle axis (the Y-axis). The clot cutting tool was ground in four steps (Figure 4.3(b)). In Step 1, the tube was tilted by $\theta = 30°$ and was plunge ground by $d = 1$ mm to create a notch on the tube. The resin bond SiC Grinding Wheel #1 was 25.4 mm in diameter and 3.2 mm in width and rotated at 10,000 rpm. In Step 2, the tube was plunge ground by $e = 0.5$ mm and $\theta = 0°$. In Step 3, the tip of the needle tube was ground to expose the cutting edge with $a = 0.2$ mm. In Step 4, the resin bond Al_2O_3 Grinding Wheel #2 (24 mm in diameter and 0.3 mm in width) cut off the clot cutting tool with a length of $l = 2.3$ mm. After these four steps, the cutting edge was honed to an edge radius $r = 40$ μm, as shown in the scanning electron microscopy (Model JSM-IT500; JEOL, Peabody, MA) image of the clot cutting tool in Figure 4.3(b).

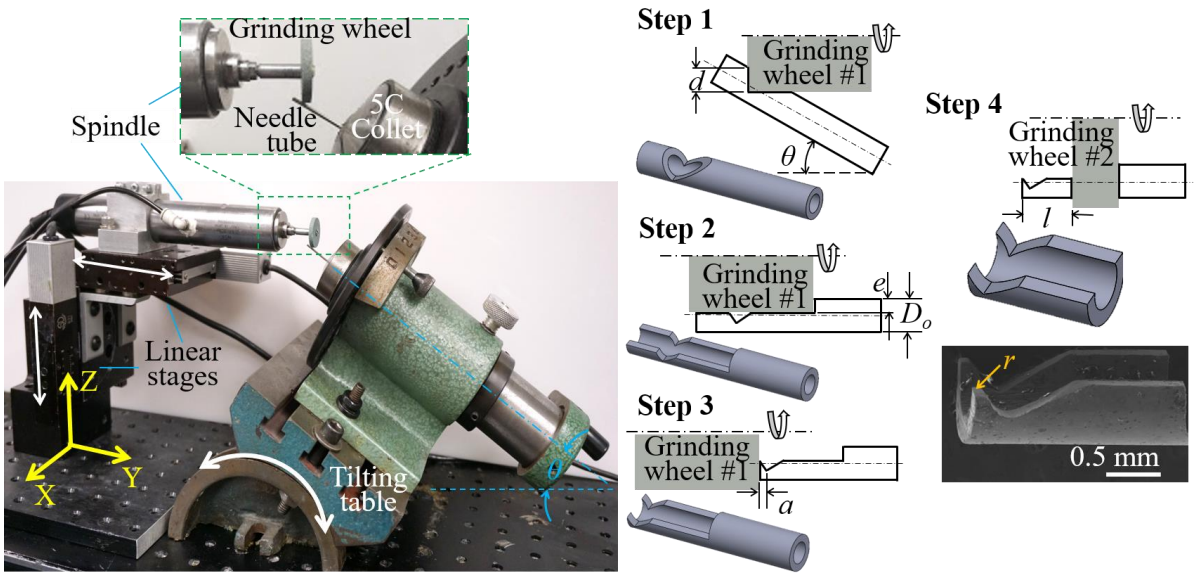

Figure 4.3 Clot cutting tool grinding: (a) grinding machine setup and (b) four steps to grind the clot cutting tool.

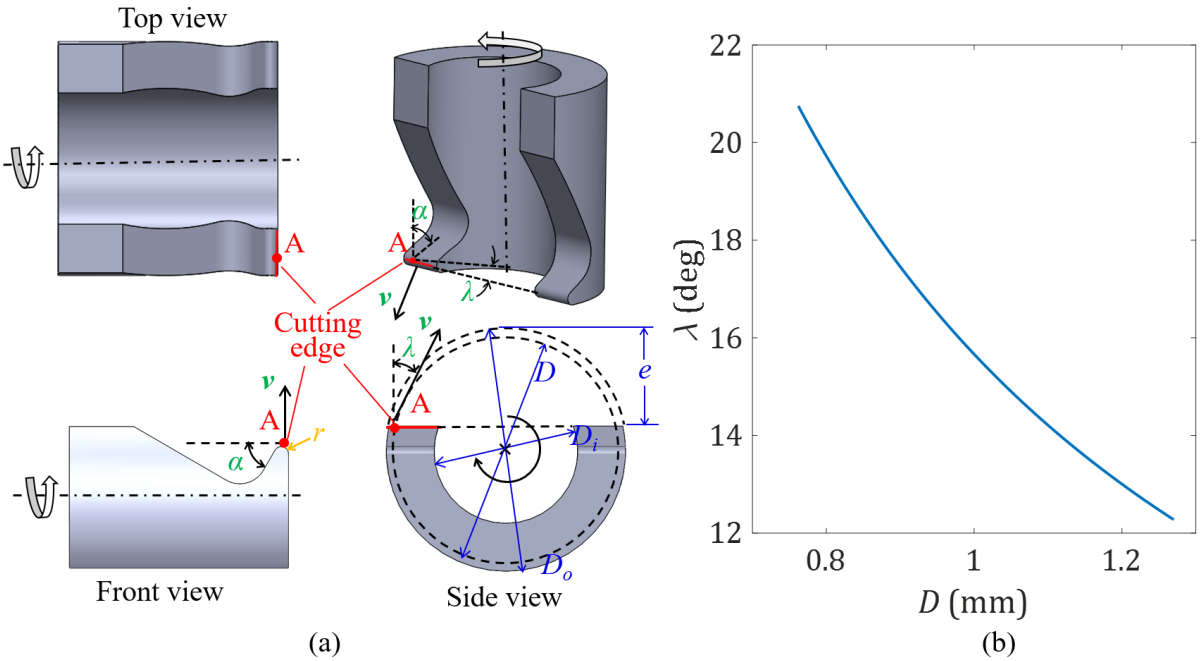

Figure 4.4 (a) Clot cutting tool and (b) inclination angle of the straight cutting edge.

Figure 4.4(a) shows the straight cutting edge with rake angle α (= 90° – θ), inclination angle λ, and cutting velocity vector $\boldsymbol{v}$ at point A, which has a radial distance of $D/2$ from the axis of clot cutting tool. The inclination angle at point A is:

$$\lambda = \sin^{-1}\left[\left(D_o - 2e\right)/D\right], D_i \le D \le D_o \tag{4.1}$$

where D_o and D_i are the outer and inner diameter of the clot cutting tool, respectively. In this study, α = 60° for high rake angle cutting of soft clots and D_o = 1.27 mm and D_i = 0.76 mm. The λ ranges from 12° to 21°, as shown in Figure 4.4(b).

4.2.3 Measurement of Cutting and Thrust Force in Clot Cutting

Figure 4.5(a) shows the cutting force (F_C) and thrust force (F_T) which are parallel and perpendicular to the cutting velocity vector, respectively. As shown in Fig. 5(b), the clot is subject to three force components, F_C, F_T, and the vacuum force (F_V) due to the vacuum suction. The force on the catheter wall is $F_T - F_V$, which is transmitted to the force transducer mounted under the water tank. The steady state force on the water tank was measured with a 1000 Hz sampling rate, neglecting the transient force component due to tool rotation. F_V was measured when the vacuum pump turned on with no cutting of the clot. The force isolator (Figure 4.2) blocked the force transmitted via the catheter and reduced the noise in $F_T - F_V$ measurement.

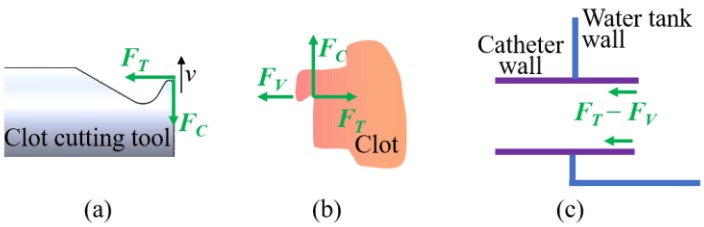

Figure 4.5 Forces on the (a) clot cutting tool, (b) clot, and (c) water tank wall.

F_C at the steady state was measured based on the change of the electric current in the motor controller with a 40 Hz sampling rate. Assuming the cutting tool rotates at a constant speed ω, $F_T = 2T / D_M$, where T is the torque on the clot cutting tool due to the clot cutting and

D_M (= 0.5(D_i+D_o)) is the mean diameter of the clot cutting tool. To find T, the motor current with and without clot cutting were measured and the difference was used to calculate $T = k\ (I - I_O)$, where k is the current to torque conversion constant and I and I_O are the motor current drawn with and without clot cutting, respectively. In this study, k = 7.05 mN-m/A was calibrated by measuring the torque of the motor shaft tip rubbing against a silicone part fixed on a piezoelectric dynamometer (Model 9271A; Kistler, Winterthur, Switzerland) and the motor current in the steady-state condition. The motor current was measured with a resolution of 0.1 mA and the resultant force resolution was 1.4 mN.

The rotating drive shaft orbits around the center of the catheter with an orbital speed Ω due to the hydrodynamic force generated by the fluid around the drive shaft [12,13]. This drive shaft orbital motion was recorded using a high-speed camera at 6000 frames per second. Over 24 frames were captured per orbital revolution for each rotational speed and used to calculate Ω.

4.2.4 Clot Workpiece

The clot was made by mixing and coagulating plasma and RBC obtained from the University of Michigan Blood Bank. To fabricate the CA, 0.05 mL of RBC was added to 10 mL of plasma. To induce coagulation, 1 mL of 2.27% calcium chloride solution was added to the mixture. During the coagulation process, the fibrinogen in the plasma was converted to fibrin network to form the highly fibrotic clot. This clot has a high tensile strength of 2.5 MPa with a similar composition and mechanical properties comparable to the strongest clot retrieved from stroke patient in Chapter 2. The blood coagulated in a 15 mm diameter, 15 mL centrifuge tube after 1.5 hours to form the clot which was cut into 5 mm long cylinders for cutting experiments. This CA had very high, close to 100%, fibrin [14] and was the most difficult-to-cut clot workpiece material due to its higher ultimate tensile strain and stress, making this CA ideal for experimental study of the effectiveness of clot cutting.

4.2.5 Experiment Design

The clot cutting tool was tested at 60,000, 90,000, and 120,000 rpm rotational speed. The drive shaft motion, motor current, and vacuum and thrust forces were recorded. Each test was repeated five times.

4.3 SPG Model for Clot Cutting

4.3.1 Model Configuration

Figure 4.6 shows the SPG model for clot cutting simulation. The model consists of the clot, clot cutting tool, water, and catheter wall. The clot was discretized with SPG particles, while the clot cutting tool and catheter wall were discretized with rigid FEM shell elements. The clot cutting tool has a rotational speed ω = 60,000, 90,000, or 120,000 rpm, with orbital speed Ω = 6840, 11,200, or 15,200 rpm, respectively, based on the high-speed camera measurement. Particles at the catheter tip are fixed.

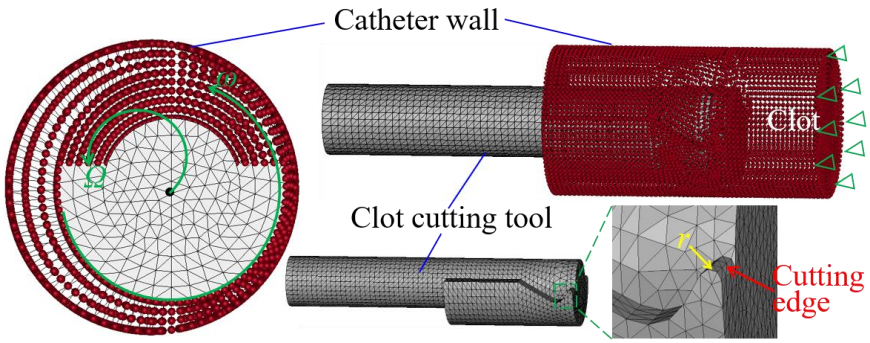

Figure 4.6 SPG model setup with blood clot and clot cutting tool.

4.3.2 Material Model and Particle Separation Criteria

The clot constitutive model was obtained through a uniaxial tensile test. The measured stress was offset by 70 kPa and the measured strain was offset by 0.51 to account for the pre-stretch of the clot due the vacuum pressure (−70 kPa) inside the catheter. The resultant stress-strain relation was fitted using a power law plasticity equation: $\sigma = k\varepsilon^n$, where σ is the true stress, k is the strength coefficient (= 14.31 MPa), n is the hardening coefficient (= 2.48), and R^2 = 0.9953. To account for the strain rate dependency of the clot property, the Cowper and Symonds model [15] was used. It scales the true stress with a factor of $1+(\dot{\varepsilon}/C)^{(1/p)}$, where $\dot{\varepsilon}$ is the strain rate, C and p are two material constants. The value of C is important to determine stress and cutting forces under the high strain rate clot deformation during cutting. In this study, a range of C was investigated while the value of p was set as 0.1.

The separation between two particles occurs when the plastic strain exceeds 0.49. The clot has a density of 1.03×10^3 kg/m^3, and a Poisson's ratio assumed to be 0.45 for the nearly incompressible clot. The friction coefficient at the clot-catheter wall and clot-cutting tool interfaces are 0.3.

4.3.3 SPG Clot Cutting Parameters

The commercial software LS-DYNA (v971 R11; Livermore Software Technology Corp; Livermore, CA) was used for the SPG modelling. The average particle-to-particle distance is 50 μm. The kernel function is cubic B-spline function with normalized dilation parameter of 1.8. The time step is about 10^{-8} s automatically calculated by the software to ensure numerical stability. The kernel function is updated every 15 time steps to mitigate the tension instability.

4.4 Results and Discussions

4.4.1 High-Speed Camera Imaging and Force Measurement Results

Figure 4.7(a) shows the high-speed camera image of the clot cutting. The chip formation was continuous, and removal was difficult. The continuous chip tangled on the drive shaft, made the chip evacuation difficult, and significantly increased the clot cutting force. Effective clot chip breakage and evacuation are important and will be talked about in Chapter 5.

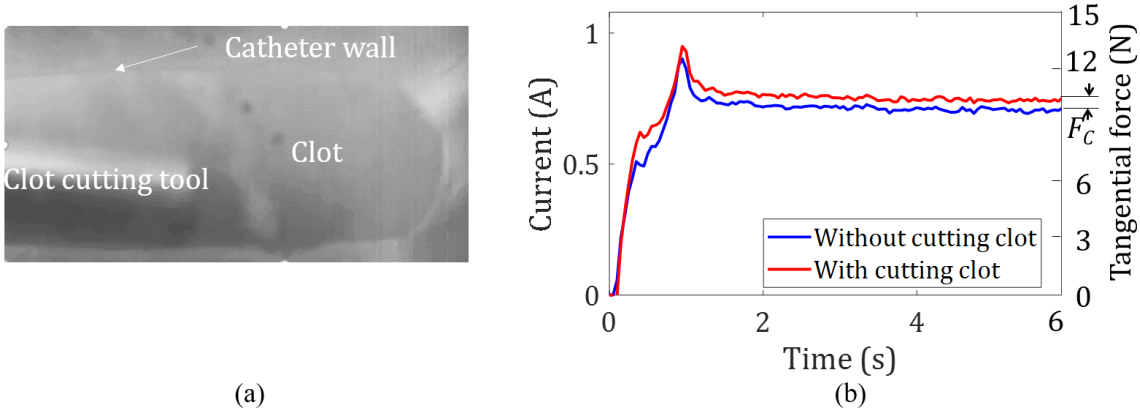

(a) (b)

Figure 4.7 (a) High speed camera imaging of the clot cutting and (b) motor current and tangential forces with and without clot cutting.

The measured motor current with and without cutting the clot was converted to the tangential forces on the clot cutting tool. The difference of steady-state tangential forces with and without clot cutting is the cutting force F_C. Figure 4.7(b) shows an example of clot cutting at 90,000 rpm. After turning on the motor at time 0, the cutting tool started to rotate and cut the clot, leading to a larger current and tangential force compared to those without clot cutting. By taking an average of the difference from 2 to 6 s (the steady state), F_C was estimated to be 0.59 N. Table 4.1 summarize the F_C at three cutting speeds. By increasing the speed of clot cutting tool from 60,000 to 120,000 rpm, F_C was reduced by half. High cutting speed is significant to lower the F_C for clot cutting.

Table 4.1 The averaged F_C, F_V, and F_T for three cutting speeds.

ω (rpm)	60,000	90,000	120,000
Fc (N)	0.74	0.59	0.36
F_V (N)	0.40	0.37	0.38
F_T (N) (assuming $F_V = 0$ during clot cutting)	0.04	0.03	0.01

Figure 4.8 shows results of $F_T - F_V$ vs. time for three clot cutting tests. The initial drop of $F_T - F_V$ was due to vacuum. The lowest point, representing the highest vacuum force (marked by red dots) on the clot, were selected to represent the F_V. The measured F_V, as shown in Table 1, is about the same, 0.37 to 0.40 N, for three cutting speeds. The clot cutting tool was turned on about 20 to 40 s after the vacuum was activated. The value of $F_T - F_V$ was increased to almost zero for all tests. The vacuum force on the clot would be lower during cutting and changed at different stages of chip formation, as shown in Figure 4.8. By assuming the vacuum force on the clot was reduced to zero during cutting (an extreme case), then F_T will be close to zero, as summarized in Table 1. Although it is difficult to predict the exact value of F_V during clot cutting, this study showed the thrust force was low in clot cutting – likely due to the free and limited constraint on the clot workpiece. The clot cutting configuration is different from traditional metal cutting with fixed workpiece support.

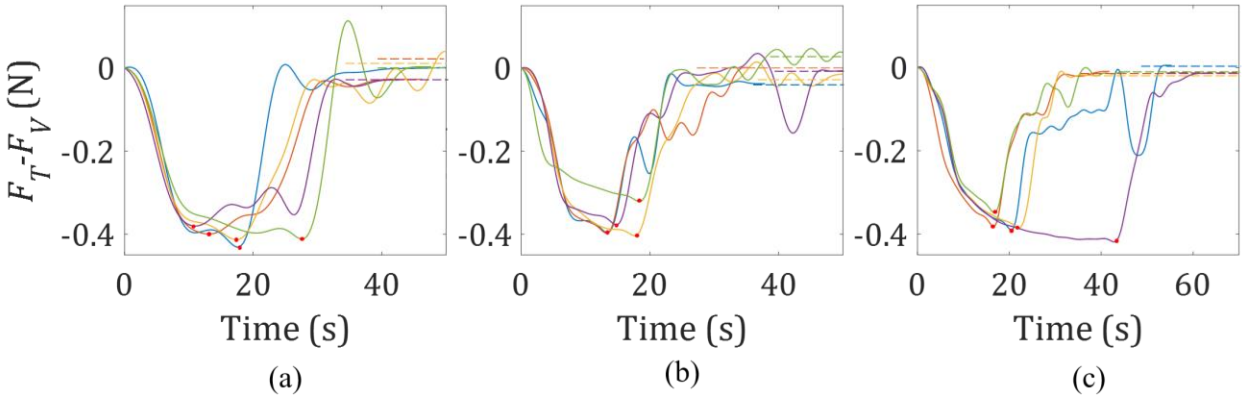

Figure 4.8 Force measurement results for $F_T - F_V$ for the rotational speed of : (a) 60,000 rpm, (b) 90,000 rpm, and (c) 120,000 rpm. The dashed lines in each figure represent the averaged F_T.

4.4.2 SPG Modelling Results

Figure 4.9(a) shows the model predicted F_C for three revolutions of clot cutting tool. The trend shows reduced F_C at a higher cutting speed. This is caused by the smaller clot-cutting tool engagement at higher cutting speeds. Compared to the value of F_C in Table 1, the SPG model predicted F_C has an error of 3%, 13%, and 20% for ω of 60,000, 90,000, and 120,000 rpm, respectively. The SPG model also showed F_T was very low (0.045 to 0.057 N), which is consistent with the experimental observation. Fig. 9(b) shows the distribution and concentration of the effective stress near the cutting edge at ω = 60,000 rpm. The value of C in the Cowper and Symonds constitutive model of the clot was studied at 1, 10, 100, and 1000 s^{-1}. C = 100 s^{-1} with the closet match to the measured forces was selected. Experimental validation of this Cowper and Symonds constitutive model for the clot will be needed by doing the Split-Hopkinson pressure bar test.

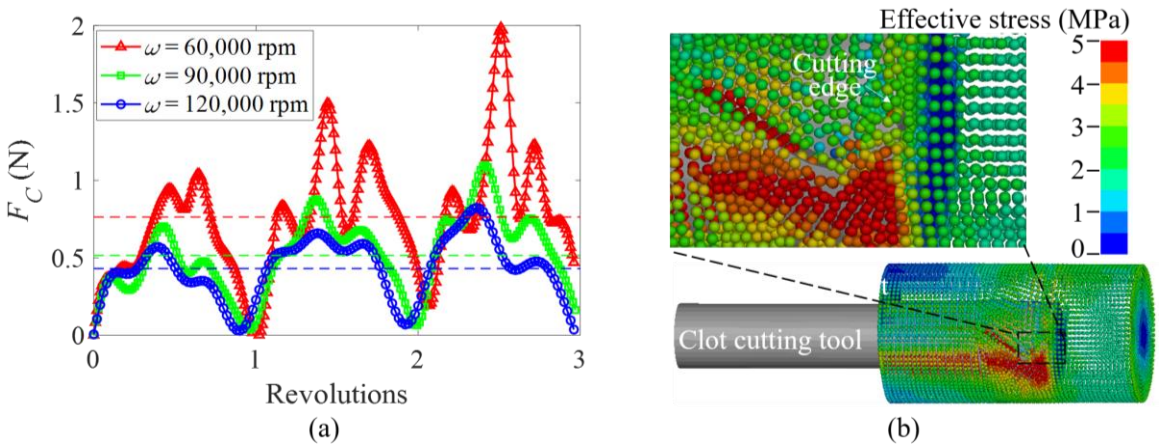

Figure 4.9 (a) SPG model predicted F_C with the time-averaged values indicated by the dashed lines and (b) the distribution of effective stress near the cutting edge for clot cutting at 60,000 rpm.

Figure 4.10 shows the comparison of the stress distribution after 0.9 revolutions of the cutting tool's rotational motion for the three cutting speeds. The stress decreases with the increase of the cutting speed, which can explain the decreased cutting force for increase cutting speed. At an increased cutting speed, the cutting tool might have smaller engagement with the clot workpiece and therefore have smaller cutting force.

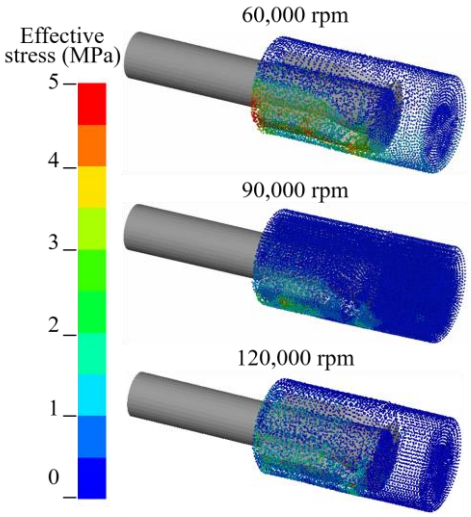

Figure 4.10 Comparison of the effective stress distribution for the three rotational speeds.

4.5 Conclusions

This study investigated the blood clot cutting mechanics via experiments and SPG modelling. The micro-grinding procedure to fabricate a miniature high rake angle clot cutting tool was developed. Three key findings from the clot cutting experiments were: 1) the tip radius of the cutting edge was important, 2) the cutting force was sensitive to cutting speed, and 3) the thrust force is low, close to zero.

4.6 References

[1] Auth DC, Clement TJ, Gordon LS (1997) Transluminal Thrombectomy Apparatus, US Patent No. 5,695,507.

[2] Moore JZ, Malukhin K, Shih AJ, Ehmann KF (2011) Hollow needle tissue insertion force model. *CIRP Annals* 60157–160.

[3] Wang Y, Van Loon M, Spangler C, Tai BL, Z Moore J, Xu Z et al. (2012) The Needle with Lancet Point – Geometry for Tip Grinding and Tissue Insertion Force. in: 7th Int. Conf. Micromanufacturing, Evanstonpp. 159–165.

[4] Liang SY, Shih AJ (2016) Analysis of Machining and Machine Tools. Springer, .

[5] Lucy L (1977) A numerical approach to the testing of the fission hypothesis. *The Astronomical Journal* 82(12):1013–1024.

[6] Gingold RA, Monaghan JJ (1977) Smoothed particle hydrodynamics: Theory and application to non-spherical stars. *Monthly Notices of the Royal Astronomical Society* 181375–389.

[7] Liu Y, Li B, Zheng Y, Shih AJ (2017) Experiment and smooth particle hydrodynamics simulation of debris size in grinding of calcified plaque in atherectomy. *CIRP Annals* 66(1):325–328.

[8] Zheng Y, Liu Y, Liu Y, Shih AJ (2019) Multigrain Smoothed Particle Hydrodynamics and Hertzian Contact Modeling of the Grinding Force in Atherectomy. *Journal of Manufacturing Science and Engineering* 141(4):041015.

[9] Belytschko T, Guo Y, Liu WK, Xiao SP (2000) A unified stability analysis of meshless particle methods. *International Journal for Numerical Methods in Engineering* 48(9):1359–1400.

[10] Morris JP (1996) Analysis of SPH with Applications, Monash University, 1996.

[11] Wu CT, Wu Y, Crawford JE, Magallanes JM (2017) Three-dimensional concrete impact and penetration simulations using the smoothed particle Galerkin method. *International Journal of Impact Engineering* 1061–17.

[12] Shih AJ, Liu Y, Zheng Y (2016) Grinding wheel motion, force, temperature, and material removal in rotational atherectomy of calcified plaque. *CIRP Annals* 65(1):345–348.

[13] Zheng Y, Liu Y, Pitre JJ, Bull JL, Gurm HS, Shih AJ (2018) Computational fluid dynamics modeling of the burr orbital motion in rotational atherectomy with particle image velocimetry validation. *Annals of Biomedical Engineering* 46(4):567–578.

[14] Duffy S, Farrell M, Mcardle K, Thornton J, Vale D, Rainsford E et al. (2017) Novel methodology to replicate clot analogs with diverse composition in acute ischemic stroke. *Journal of NeuroInterventional Surgery* 9(5):486–491.

[15] Snedeker JG, Niederer P, Schmidlin FR, Farshad M, Demetropoulos CK, Lee JB et al. (2005) Strain-rate dependent material properties of the porcine and human kidney capsule. *Journal of Biomechanics* 38(5):1011–1021.

CHAPTER 5
BUBBLE GENERATION, CLOT CHIPS MOTION, AND CAVITATION IN A CLOT CUTTING CATHETER

5.1 Introduction

Bubbles and clot chips are generated inside the clot-cutting catheter and pose a safety concern for the stroke patients by using the clot-cutting catheter. As shown in Figure 2.1(a), the rotating cutting tool cuts the clot to form clot chips. The high-speed camera has observed bubbles generated near the tool, as shown in Fig. 2.1(b). During the mechanical thrombectomy procedure, if bubbles flow out of the catheter, the brain vessels will be occluded. This is called air embolism [1],. Air embolism is most commonly seen in inserting and removing a catheter and has a 0.13% incidence rate in the insertion of central venous catheters [2]. Air embolism in the brain vessels can lead to severe neurologic deficits and possible death [3]. For the clot chips, they can also block the blood flow and cause embolization. Embolization also exists for the current commercially available mechanical thrombectomy devices with an incidence rate of about 10% for the stent retriever [4]. Understanding the bubble generation mechanism and how the clot chips travel with the flow inside the catheter is needed to mitigate the risks of air embolism and embolization.

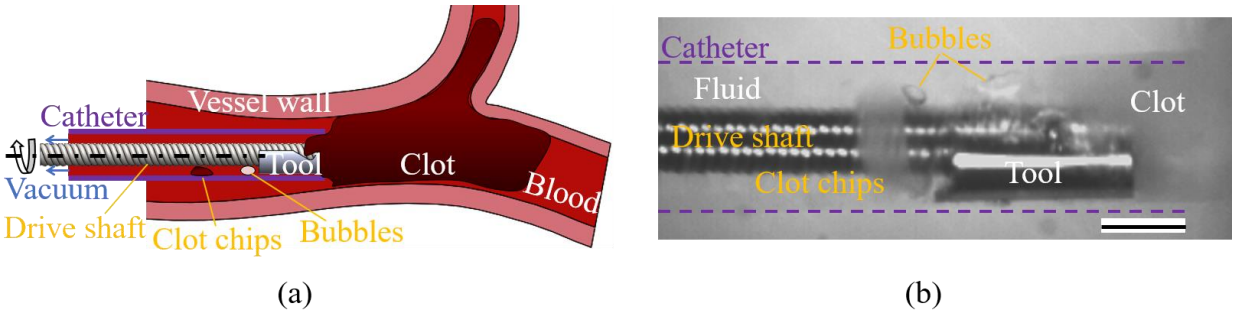

(a) (b)

Figure 5.1 Clot chips and bubbles generated inside the clot cutting catheter: (a) schematic and (b) high-speed camera image for 60,000 rpm cutting speed. Scale bar = 1 mm.

Air bubbles may be generated from cavitation inside the catheter. Cavitation is a nucleation process when the fluid pressure drops lower than its vapor pressure to create bubbles filled with vaporized fluid. Cavitation can be induced by either increasing the vapor pressure using heat or reducing the flow pressure using acoustics or centrifugation [5]. As first reported by Reynolds [6], cavitation can also happen with the hydrodynamic flow where the fluid pressure is reduced around a fast moving object immersed in the fluid. In water, the bubbles will form by cavitation under –99 kPa at 20^{o}C [7]. The collapse of the bubbles can release energy and has been applied to emulsify biological tissue such as kidney stones, gall stones, and cancer cells [8]. Cavitation can also be induced by high-intensity ultrasound pulsed and used to fragment clots within *in vitro* models [9,10]. This study will explore to use the cavitation to fragment clot chips.

Fluid flow of a rotating and orbiting object inside a cylinder has been studied both experimentally and numerically. Experimentally, particle image velocimetry (PIV) was applied to study the rotating 3D prolate spheroid inside a opened cylinder for the rotational atherectomy [11]. Numerically, the 2D fluid flow in the gap between two eccentric cylinders with the inner cylinder rotating and orbiting has been studied by Feng et al. [12]. The hydraulic force increases with the inner cylinder surface speed, leading to a higher orbital speed. Similar findings have been studied for the case without the inner cylinder orbiting [13] and also for the rotational atherectomy [11], which reported a lowest pressure of –30 kPa.

In this study, the bubble generation mechanism and the clot chips motion were studied using a high-speed camera and a 3D CFD model. The cutting tool induced cavitation will be studied by the CFD model only. This chapter is organized as follows: the experimental setup

and the formulation of the CFD model are first introduced. The experimental results for the bubble generation and the clot chips motion are then presented, followed with the CFD results.

5.2 Experimental Setup

5.2.1 Clot Removal Device and Measurement Setup

The clot removal device consisted of a motor drive unit, a clot cutting catheter, and a vacuum pump. As shown in Figure 5.2, the drive unit rotated a flexible drive shaft (0.51 mm inner and 0.76 mm outer diameter) inside a 1.32 m long transparent catheter (1.59 mm inner diameter). The proximal end of the drive shaft was connected to the drive unit and the distal end was placed at the tip of the catheter.

Inside the drive unit, a telescoping system was used to allow the rotational motion and translational motion of the drive shaft. The drive shaft was driven by an electric motor and rotated inside the drive shaft assembly and entered a stationary guide through a ring seal. The guide was a hollow tube that allowed the shaft to move translationally. The guide inner dimeter was larger than the outer dimeter of the drive shaft assembly and a ring seal was used to minimize the air leaking into the guide. The guide was connected to a hemostasis Y-shaped valve (Model FLO50; Merit Medical, South Jordan, Utah), with the other end of the valve connected to the catheter. One branch of the Y-shaped valve was connected to a vacuum pump (Model 01-12-405; Allied Healthcare, St. Louis, MO) to generate the vacuum pressure. The vacuum pressure from the pump was set as −650 mmHg (−87 kPa, gauge pressure) while the vacuum at the catheter tip was smaller, −70 kPa, which was measured by a pressure sensor (Model 015PDAA5, Honeywell, Charlotte, NC). This difference could be due to the leaking through the non-perfect ring seal in the drive unit, as shown in Figure 5.2.

At the tip of the catheter, the flow motion was captured using a high-speed camera. The tip of the catheter was placed inside a water tank with the clot at the front. Upon activation of the vacuum pump, the water and the clot were drawn into the catheter tip. A high-speed camera (Model FASTCAM-1024PCI; Photron, San Diego, CA) was used to acquire images of the clot

removal process at 10,000 frames per second. The catheter was illuminated by a halogen light-source (Model 8375; Fostec, Mainz, Germany).

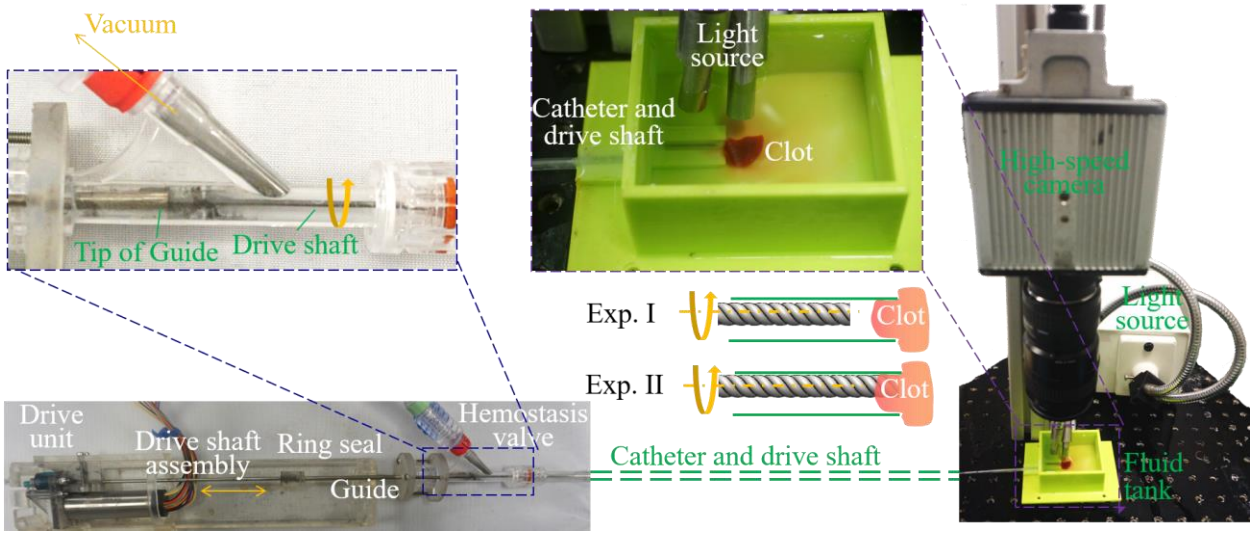

Figure 5.2 Experimental setup.

Two experiments (marked as Exp. I and Exp. II) were carried out to study the bubble generation and clot chips motion inside the clot-cutting catheter. As shown in Figure 5.2, in Exp. I, without cutting the clot, the bubble generation was studied at the tip and around the drive shaft. After the vacuum drew the clot into the catheter tip, the drive shaft was pulled back to form a small gap (about 1 mm) from the clot. The bubble generation and transformation after the catheter tip was plugged by the clot was recorded. In Exp. II, the clot was cut, and the motion of chips was studied. After the vacuum drew the clot into the catheter tip, the drive shaft was positioned to engage with and fragment the clot. Right after the clot was fragmented by the catheter, the motion of the clot chips was observed using the high-speed camera. For both Exps. I and II, the drive shaft rotational speed was 60,000 rpm. Before each experiment, the vacuum was activated for 10 seconds without clot in front of the catheter tip to draw the water into the catheter to remove all the air within the catheter.

5.2.2 Clot Analog

The CA was made by mixing and coagulating plasma and RBC obtained from the University of Michigan Blood Bank, as described in Chapter 3. To fabricate the CA, RBC,

plasma and 2.27% calcium chloride solution were mixed with a 1:9:1 volume ratio [14,15]. The CA was formed in a 15 mm diameter, 15 mL centrifuge tube for 1.5 hours and then cut into 5 mm long cylinders for experiments.

5.3 CFD Modelling

5.3.1 Model Configuration

A CFD model was developed to study the fluid field inside the catheter. Figure 5.3(a) shows the CFD model configuration. The model consists of the fluid domain inside the catheter (Zone A), and outside the catheter (Zone B). The proximal end of the proximal end of the catheter lumen is set as a pressure outlet with $P_{out} = -70$ kPa. In Zone B, the fluid domain is a cuboid with the bottom face having a wall boundary condition and the other faces having a pressure boundary of $P_{in} = 0$ kPa.

The flow domain was discretized with 1.68 million hexahedron and 60,000 pyramid cells using the software Pointwise (v18, Pointwise Inc., Fort Worth, TX, USA). The average cell edge length was about 40 μm. As shown in Figure 5.3(b), finer hexahedrons with 18 μm cell height were used to resolve the boundary layer.

The CFD model has two stages to simulate the transition from clot occluding the catheter tip (Stage 1) to clot removed (Stage 2), as shown in Figure 5.3(c). In Stage 1, as the clot is drawn into the catheter tip, the catheter tip is set as a wall boundary condition to simulate the occluding of the catheter tip by the clot. Only the flow field in Zone A is modelled and the steady state solution is used as the initial condition of Stage 2. In Stage 2, as shown in Figure 5.3(d), after the clot is removed, the catheter tip is opened and the wall boundary condition at the catheter tip is replaced with an interior interface and the flow field in both Zone A and Zone B are computed.

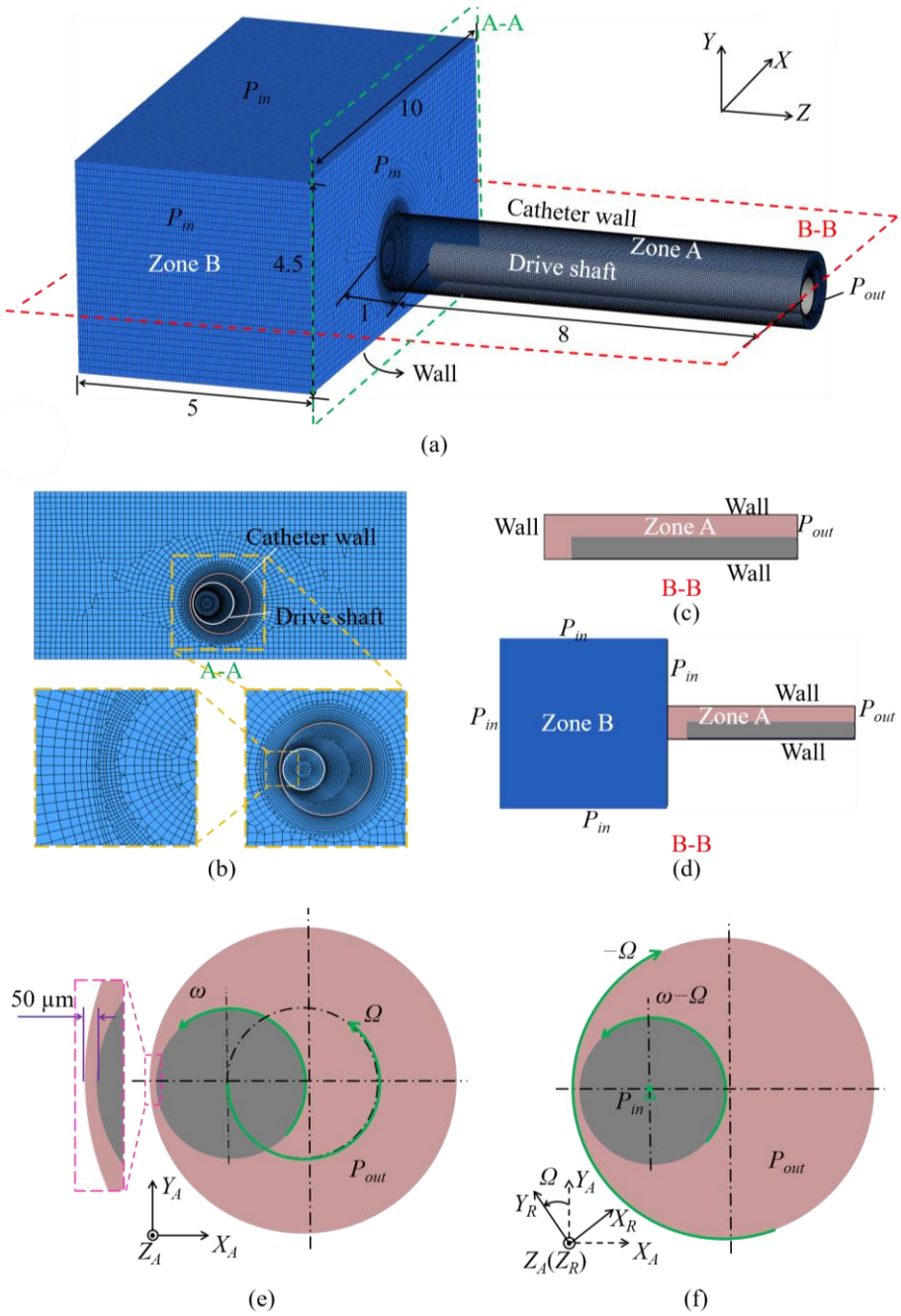

Figure 5.3 (a) CFD model configuration, (b) cross-sectional view of the mesh (c) computed domain in Stage 1, (d) computed domain in Stage 2, and drive shaft and catheter wall boundary conditions: (e) in a inertial reference frame and (f) in a rotating reference frame. (Unit: mm).

As shown in Figure 5.3(e), a rotating reference frame was introduced to simulate the drive shaft orbital motion in Zone A. By neglecting the translational motion along the length of the drive shaft, the drive shaft rotates around its center at a speed of ω and orbits around the

center of the catheter at a speed of Ω due to the hydrodynamics force exerted by the surrounding fluid [11]. As the drive shaft orbits, the shape of Zone A changes and the mesh needs to be continuously updated to discretize Zone A, demanding high computing power. To avoid this, a rotating reference frame was introduced [11,12]. As shown in Figure 5.3(f), in the rotating reference frame with a speed of Ω, the drive shaft has a rotational speed of $\omega - \Omega$ and the catheter wall has a rotational speed of $-\Omega$. In this study, ω = 60,000 rpm and Ω = 14,720 rpm based on the high-speed camera measurement. For Zone B, the fluid was computed on the inertial reference frame. Both the catheter wall and drive shaft wall are assumed to be rigid and have non-slip condition. The drive shaft was assumed to be a smooth cylinder and a gap of 50 μm, which is the averaged groove depth of the drive shaft, was introduced between the drive shaft and the catheter wall.

Another model was developed to study the cavitation induced by the rotating cutting tool. In this model, the inner cylinder was replaced with the drive shaft with the cutting tool, the same geometry studied in Chapter 4. The cutting tool rotational speed was 60,000 rpm by prescribing velocity to the surface mesh of the cutting tool. For this model, P_{out} = −90 kPa was used to assume a case with stronger vacuum power and better ring seal.

5.3.2 Numerical Method

The flow field near a rotating cylinder inside another cylinder is the canonical Taylor-Couette flow. To determine the turbulent effects, the Taylor number, *Ta*, was calculated [16]:

$$Ta = R_I \omega^2 (R_O - R_I)^3 / \nu^2 \tag{5.1}$$

where R_O and R_I are the radius of the catheter lumen (= 0.79 mm) and the radius of the drive shaft (= 0.38 mm), ν is the kinematic viscosity of water (= 1.00×10^{-6} m^2/s). In this study, *Ta* = 1.05×10^6, over 600 times the critical Taylor number (= 1708) [17], indicating the flow was in the turbulent flow regime [18]. To solve the turbulence, the re-normalization group k–ε turbulence model was used. This model was also used to solve the turbulent flow for the rotational atherectomy with turbulent Taylor-Couette flow [11].

The 3D incompressible and isothermal Navier-Stokes equations were solved using the CFD software, Fluent (v19.1; ANSYS, Canonsburg, PA). The second order scheme was applied to discretize the pressure and momentum and the Semi-implicit pressure linked equations were utilized to handle the velocity-pressure coupling. The convergence criterion was 10^{-3} for the residuals of continuity, momentum, and turbulent transport equations. For the transient simulation for Stage 2, the time step was 10^{-5} s.

5.4 Results

5.4.1 Experimental Results: Exp. I Bubble Generation

Figure 5.4(a) shows the generation, motion, and transformation of a single bubble. The video was taken 2.5 seconds after the shaft started to rotate. At t = 0, the clot plugged the catheter tip and the rotating drive shaft was 1 mm away from the clot. At t = 0.5 ms, a bubble was observed to emerge from the proximal side of the drive shaft while attached to the drive shaft. The bubble rotated with the drive shaft and kept moving translationally toward the drive shaft distal end until reaching the drive shaft distal end at t = 8.8 ms. The bubble collapsed and formed three smaller bubbles at t = 10.2 ms. Those smaller bubbles coalesced into a single bubble at t = 16 ms and another bubble emerged from the proximal side of the drive shaft.

Figure 5.4(b) shows the growth of the bubbles inside the catheter. All the bubbles emerged from the proximal side of the drive shaft and traveled to the drive shaft tip. The bubbles coalesced into bigger bubbles until at t = 2.4 s, a large bubble was formed surrounding the drive shaft and the bubble size stabilized.

All the bubbles were caused by air entering the catheter tip through the ring seal inside the drive unit. The bubbles cannot be caused by cavitation since the flow pressure was higher than the vapor pressure of the water (−99 kPa at 20^{o}C), as will be presented in the CFD modelling results section.

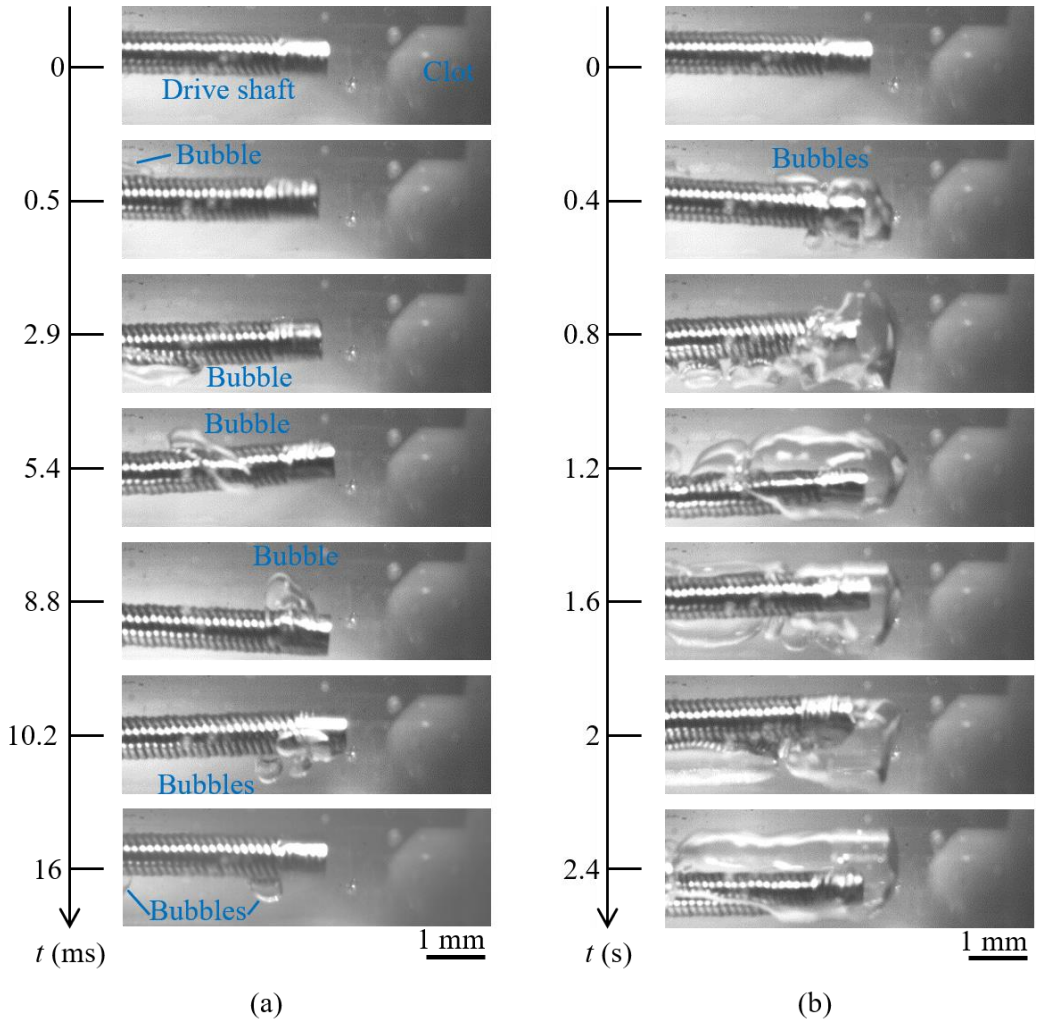

Figure 5.4 (a) Generation, motion, and transformation of a single bubble and (b) growth of bubbles inside the catheter.

5.4.2 Experimental Results: Exp. II Clot Chips Motion

Figure 5.5 shows the clot chip motion right after the clot was fragmented in the catheter. At $t = 0$, the clot chip was about to detach from the drive shaft. The clot chip then moved out of the catheter tip. At $t = 2$ ms, the clot chip flowed out of the camera view.

The flow speed was estimated using the trajectory of the clot chip. The accurate flow velocity vector cannot be confidently determined due to the out-of-plane motion of the flow field captured by the high-speed camera. For the clot chip shown in Figure 5.5, speed of clot was estimated to be about 1.7 m/s.

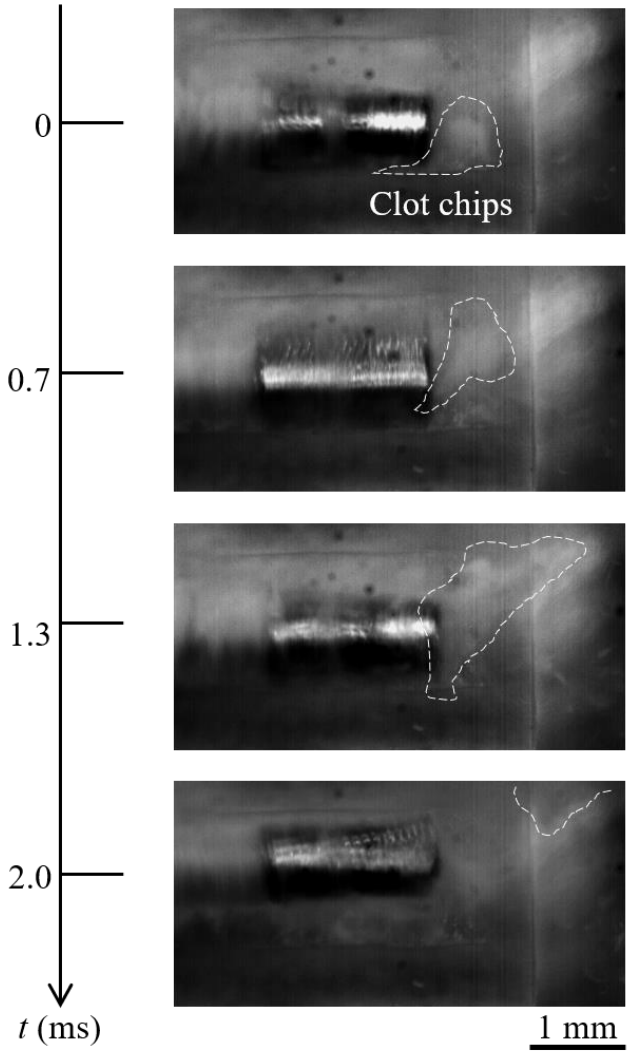

Figure 5.5 Clot chips detached from the drive shaft and flow out of the catheter.

5.4.3 CFD Modelling Results

Figure 5.6 shows the flow field for Stage 1 from the CFD modelling result. The rotational motion of the drive shaft created strong circulating flow in the surrounding fluid. As shown in Figure 5.6 (a), a pair of counter-rotating vortices were observed and such flow pattern has been reported as the eccentric Taylor-Couette flow [19]. The drive shaft rotational motion also created pressure difference across the gap between the drive shaft and the catheter wall, as shown in Figure 5.6(b). Such pressure difference drove the drive shaft to do orbital motion. The lowest pressure was around −71 kPa and was near the drive shaft surface with the azimuthal position $\theta = \pi$. This lowest pressure is greater than the water vapor pressure (−99 kPa) so

cavitation did not exist for the clot cutting catheter and the bubbles observed in Exp. I was likely initiated from the air leakage at the ring seal, as shown in Figure 5.2.

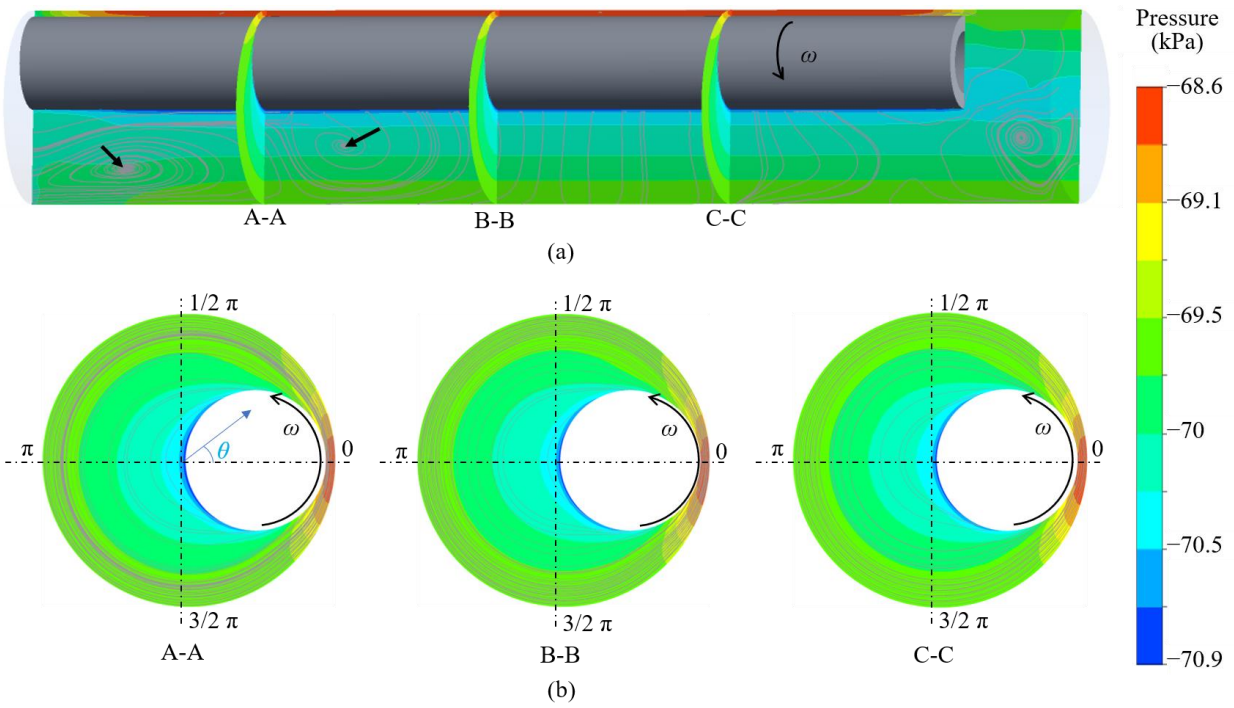

Figure 5.6 Pressure distributions inside the clot cutting catheter: (a) axial view and three cross-sectional views of pressure and surface streamlines and (b) three cross-sectional views of pressure and surface streamlines. The Taylor-Couette vortex pair are labelled by the black arrows.

Figure 5.7 shows the flow field with the contour plot of the velocity *w* in the *Z*-direction (along the length of the catheter) and the flow vector field for Stage 2 from the CFD modelling result. At $t = 0$, the clot was removed and the fluid inside both Zone A and Zone B has negligible *w*. After that, the water started to flow into the catheter and *w* was mostly negative across Zone A and Zone B. Positive *w* was found at the corner of the catheter, where the circulating flow pattern was developed. The value of *w* was around 2 m/s, similar to that of the clot chip speed (1.7 m/s) estimated from the high-speed camera. With such circulating flow, clot chips that are generated but not effectively evacuated by the vacuum can flow out of the catheter and cause embolization.

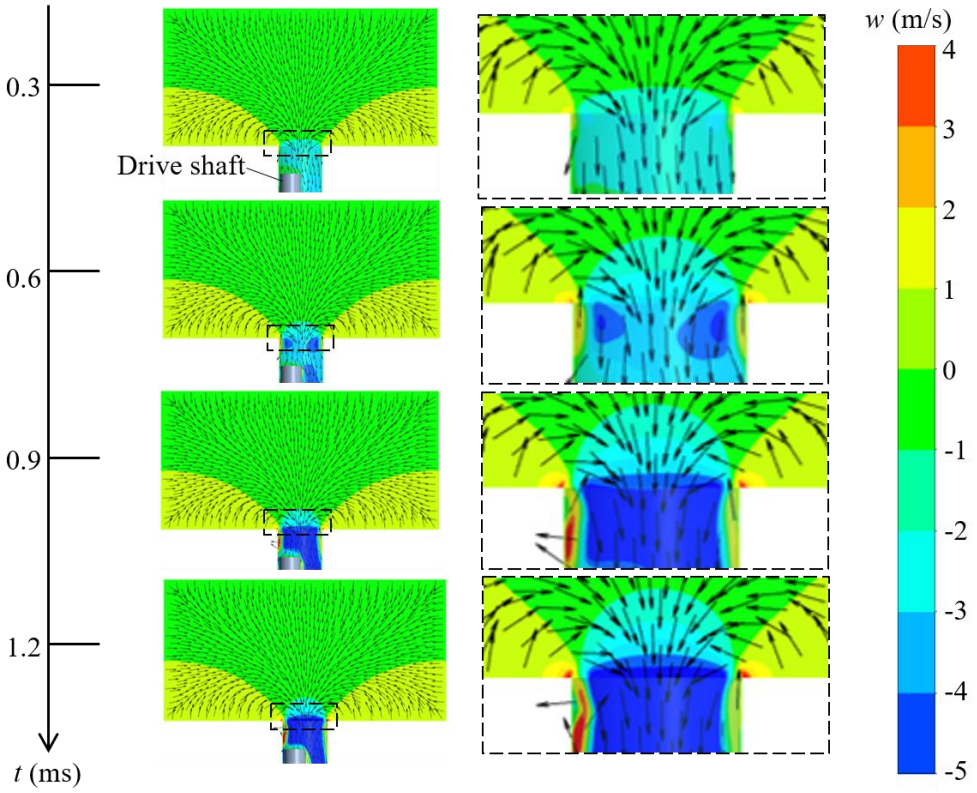

Figure 5.7 Contour plot of the flow speed *w* and the vector field for different time instances in Stage 2.

To mitigate the embolization risk, good clot chip evacuation is needed, and cavitation can be induced to fragment the clot chips to better evacuate the clot chips by vacuum. Figures 5.8 (a) and (b) show the flow field near the catheter tip with the pressure distribution and surface streamlines at different cross-sections for the drive shaft rotational speeds of 60,000 rpm and 200,000 rpm, respectively. As shown by the streamlines in Figure 5.7(a), a vortex was formed proximal to the cutting edge due to the flow separation as the flow "step down" from the surface of the cutting tool to the surface to the drive shaft. The center of the vortex had a low pressure of −91.5 kPa, 1.5 kPa lower than P_{out}. This effect of reducing the pressure was stronger than that for the rotating cylinder shown in Figure 5.6, which was only 0.9 kPa.

The lowest pressure reduced as the rotational speed increased. As shown in Figure 5.7(b), at a rotational speed of 200,000 rpm, the lowest pressure was −98.6 kPa, very close to the vapor pressure (−99 kPa) of water. At this rotational speed, cavitation is possibly to happen and

can be used to fragment the clot chips to achieve better chip evacuation and mitigate the risk of embolization.

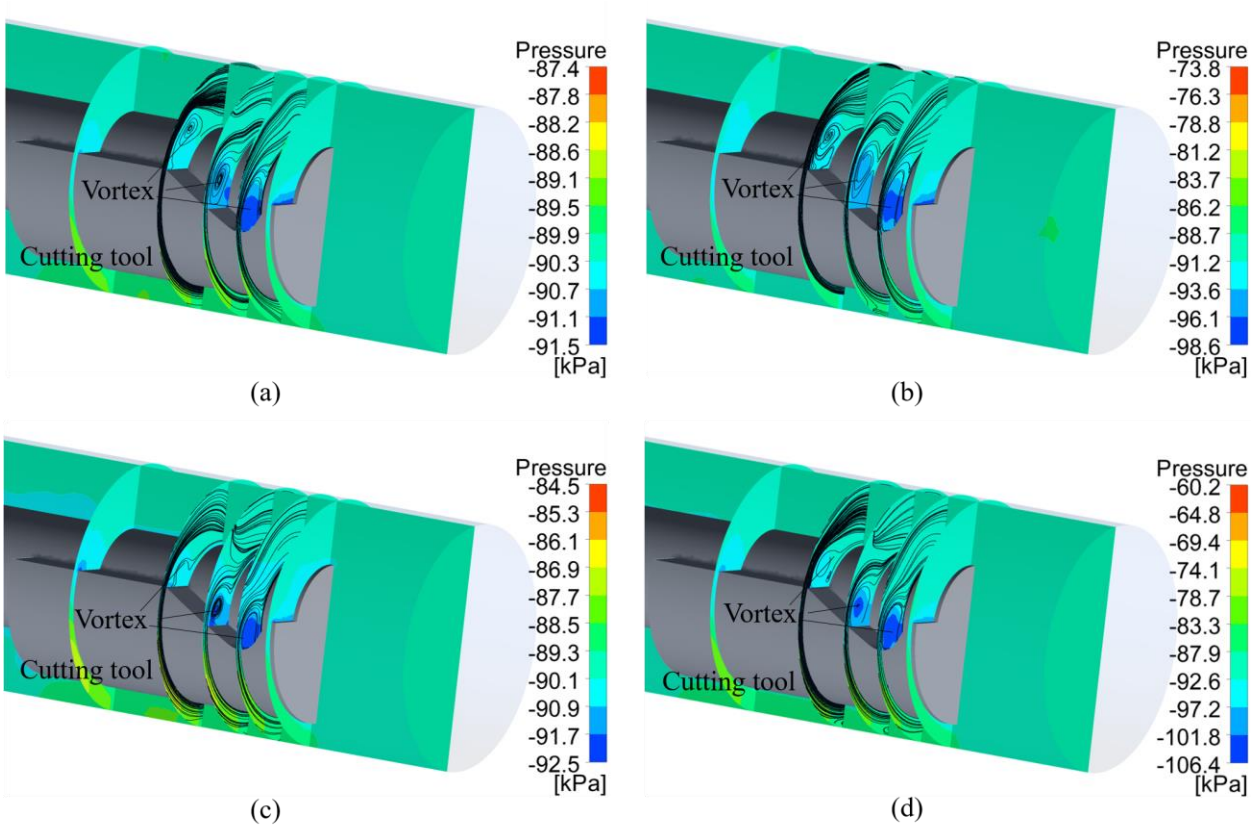

Figure 5.8 Contour plot of the pressure and the surface streamlines for the flow near the catheter tip with: (a) water at 60,000 rpm, (b) water at 200,000 rpm, (c) blood at 60,000 rpm, and (d) blood at 200,000 rpm.

Another two cases with blood inside the catheter were modelled to study the cavitation under the clinical setting. The blood density was 1.06×10^3 kg/m^3 and the blood viscosity was described by a power law model [20]:

$$\mu = 3.5\times10^{-3}\dot{\gamma}^{-0.4}, 10^{-9}\ \text{s}^{-1} \le \dot{\gamma} < 327\ \text{s}^{-1} \tag{5.2}$$

where μ is the dynamic viscosity $\dot{\gamma}$ is the shear strain rate. For $\dot{\gamma} < 10^{-9}$ s^{-1}, μ = 0.555 Pa·s and for $\dot{\gamma} \ge 327$ s^{-1}, $\mu = 3.45\times10^{-3}$ Pa·s.

As shown in Figures 5.8 (c) and (d), the lowest pressure was −92.5 kPa and −106.4 kPa, 1 kPa and 7.8 kPa lower than those with water inside the catheter, for the rotational speeds of 60,000 rpm and 90,000 rpm, respectively. This could due to a stronger vortex as a result of a stronger flow separation for the case with the blood. The blood, compared to the water, had higher viscosity and therefore a thicker boundary layer. The high-speed flow inside the boundary layer separated from the cutting tool surface and created a stronger vortex for the blood. Compared to water, cavitation can be induced at a lower tool rotational speed for the blood. These results show the current rotating tool design in this study can induce cavitation to break clot chips when applied to a real stroke patient.

5.5 Conclusions

Bubbles and clot chips were generated inside the clot-cutting catheter and posed embolization risks to the patients. The bubbles were induced by the air leakage from the ring seal inside the drive unit and could be minimized by a better seal. Clot chips were accumulated near the catheter tip and can be pushed out of the catheter due to the recirculating flow near the catheter tip. To reduce the chip accumulation, the clot chips could be fragmented by cavitation induced by the low-pressure vortex core downstream the cutting edge.

5.6 References

[1] Gordy S, Rowell S (2013) Vascular air embolism. *International Journal of Critical Illness and Injury Science* 3(1):73–76.

[2] Vesely TM (2001) Air Embolism during Insertion of Central Venous Catheters. *Journal of Vascular and Interventional Radiology* 12(11):1291–1295.

[3] Mishra R, Reddy P, Khaja M, Presentation C (2016) Fatal Cerebral Air Embolism: A Case Series and Literature Review. *Case Reports in Critical Care*3425321.

[4] Costalat V, Lobotesis K, Machi P, Mourand I, Maldonado I, Heroum C et al. (2012)

Prognostic factors related to clinical outcome following thrombectomy in ischemic stroke (RECOST Study). 50 patients prospective study. *European Journal of Radiology* 81(12):4075–4082.

[5] Caupin F, Herbert E (2006) Cavitation in water : a review. *C. R. Physique* 7:1000–1017.

[6] Reynolds O (1900) Experiments showing the boiling of water in an open tube at ordinary temperatures. *Scientific Papers on Mechanical and Physical Subject* 2578–587.

[7] Cengel Y, Boles M (2010) Thermodynamics: An Engineering Approach. 7th ed. McGraw-Hill Higher Education, .

[8] Brennen CE (2015) Cavitation in medicine. *Interface Focus* 5:20150022.

[9] Goudot G, Mirault T, Arnal B, Boisson-Vidal C, Le Bonniec B, Gaussem P et al. (2017) Pulsed cavitational therapy using high-frequency ultrasound for the treatment of deep vein thrombosis in an in vitro model of human blood clot. *Physics in Medicine and Biology* 62(24):9282–9294.

[10] Maxwell A, Cain C, Duryea A, Yuan L, Gurm H, Xu Z (2009) Non-Invasive Thrombolysis Using Pulsed Ultrasound Cavitation Therapy – Histotripsy. *Ultrasound in Medicine & Biology* 35(12):1982–1994.

[11] Zheng Y, Liu Y, Pitre JJ, Bull JL, Gurm HS, Shih AJ (2018) Computational fluid dynamics modeling of the burr orbital motion in rotational atherectomy with particle image velocimetry validation. *Annals of Biomedical Engineering* 46(4):567–578.

[12] Feng S, Li Q, Fu S (2007) On the orbital motion of a rotating inner cylinder in annular flow. *International Journal for Numerical Methods in Fluids* 54(2):155–173.

[13] Podryabinkin E V., Rudyak VY (2011) Moment and Forces Exerted on the Inner Cylinder in Eccentric Annular Flow. *Journal of Engineering Thermophysics* 20(3):320–328.

[14] Duffy S, Farrell M, Mcardle K, Thornton J, Vale D, Rainsford E et al. (2017) Novel methodology to replicate clot analogs with diverse composition in acute ischemic stroke. *Journal of NeuroInterventional Surgery* 9(5):486–491.

[15] Liu Y, Zheng Y, Li AD, Liu Y, Savastano LE, Shih AJ (2019) Cutting of blood clots – Experiment and smooth particle Galerkin modelling. *CIRP Annals*.

[16] Wei BT, Kline EM, Woodruff SHLEEANDS (1992) Gortler vortex formation at the inner cylinder in Taylor-Couette flow. *Journal of Fluid Mechanics* 245:47–68.

[17] Davey A (1962) The growth of Taylor vortices in flow between rotating cylinders.

Journal of Fluid Mechanics 14(3):336–368.

[18] Dong S (2007) Direct numerical simulation of turbulent Taylor-Couette flow. *Journal of Mechanics* 587373–393.

[19] Leclercq C, Pier B, Scott JF, Leclercq C, Pier B, Scott JF et al. (2014) Absolute instabilities in eccentric Taylor-Couette-Poiseuille flow. *Journal of Fluid Mechanics* 741:543–566.

[20] Jozwik K, Obidowski D (2010) Numerical simulations of the blood flow through vertebral arteries. *Journal of Biomechanics* 43(2):177–185.

CHAPTER 6
CONCLUSIONS AND FUTURE WORK

6.1 Conclusions and Major Contributions

This dissertation studied the workpiece properties and cutting mechanics for clot removal in cerebral arteries by an innovative mechanical thrombectomy device. Experiments were conducted to characterize the tensile properties and composition of the clots from stroke patients and CAs were fabricated with similar tensile and histological properties with those of the patient clots. An innovative mechanical thrombectomy device was built with a miniature cutting tool for difficult-to-remove clots. A clot cutting model was established to predict the force components and validated by experiments. Safety risks for the device was identified and risk mitigation strategies were proposed based on experiment observations and the fluid model.

The major achievements of this dissertation are:

(1) *A methodology to test the stroke patient clots and make realistic CAs*: The mechanical properties of the stroke patient clots were characterized by tensile test and the composition was examined by histology. Clots from stroke patients are highly-regulated and access-limited. To replace the highly access-limited stroke patient clots, clots analog with similar compositions and mechanical properties were fabricated and the CA allowed the investigation of the interaction between the mechanical thrombectomy devices and the clots.

(2) *An experiment setup to investigate the cutting mechanics for the clot-cutting catheter*: An experiment setup was built with the clot-cutting based mechanical thrombectomy device, the CA, and the force and motion measurement system. The tool and fluid

motion and cutting forces can be measured to study the interaction between the cutting tool, clot, and the fluid. High sampling rate of the high-speed camera enabled the visualization of the high-speed cutting process. This setup could be exploited for testing other cutting tool geometries and device designs.

(3) *A soft tissue cutting numerical model to estimate the cutting force on the clot*: A cutting simulation using the SPG method was carried out and validated by the experiment. The clot workpiece material property was measured using the tensile test and the strain rate effect was studied using a Cowper and Symonds model. The cutting, especially for soft tissue cutting with large plastic strain, is one of the most challenging modelling problems for traditional finite element method due to the numerical failure induced by the large deformation and material fracture. The SPG model proposed in this thesis study is the first on soft tissue cutting.

The original discoveries and key conclusions of this dissertation can be summarized as follows:

(1) The current commercially available mechanical thrombectomy devices apply tensile load to the clot and the removal completeness and embolization rate are related to the tensile strength of the clot. Tensile test is a clinically most relevant test method.

(2) Clots causing strokes are highly heterogeneous, both mechanically and histologically, from patient to patient and within the same patient. Mechanically, clots have a large range of ultimate tensile strain ranging from 1.05 to 4.89, and ultimate tensile stress ranging from 63 to 2396 kPa. Histologically, clots have 0.45% to 91% (43%±35%) RBC, 0 to 95% (40%±37%) fibrin, and 1.7% to 56% (18%±16%) platelets.

(3) For the clots obtained from stroke patients, the ultimate tensile strain is strongly and positively correlated with the platelet percentage. The ultimate tensile stress is moderately and negatively correlated with the RBC percentage, and strongly and positively correlated with the fibrin percentage.

(4) CA mimicking the composition and tensile property of the stroke patient clots can be made by mixing RBC, plasma, and platelets in different ratios and the histological composition of the CA can be predicted by a regression model ($p < 0.001$).

(5) For the CA, the elastic modulus is strongly and negatively correlated with RBC percentage, strongly and positively correlated with fibrin percentage. The ultimate tensile strain is moderately and negatively correlated with the RBC percentage and moderately and positively correlated with the fibrin percentage. The ultimate tensile stress is strongly and negatively correlated with the RBC percentage and strongly and positively correlated with the fibrin percentage.
(6) For the clot with near 100% fibrin, the cutting force is 0.74, 0.597, and 0.36 N for the rotational speed of 60,000, 90,000, and 120,000 rpm, respectively.
(7) The thrust force is small (0.01 – 0.04 N) since the clot workpiece is not well supported and is suspended in the fluid.
(8) The SPG model predicted cutting force has an error of 3%, 13%, and 20% for the rotational speed of 60,000, 90,000, and 120,000 rpm, respectively.
(9) Bubbles and clot chips can be found at the catheter tip during clot cutting and the risks of them flowing out of the catheter can be mitigated by a better seal for the device and the rotation-induced cavitation near the cutting edge.

These findings and lay the groundwork for developing effective and safe mechanical thrombectomy devices. Utilizing the knowledge of clot property and the experiment and modelling tools, new device can be developed to be applied for the treatment of not only stroke, but also myocardial infarction, pulmonary embolism, and deep vein thrombosis.

6.2 Future Work

The experimental setup and models proposed in this dissertation could be further improved and extended in the following directions:

(1) The CA and the SPG model can be applied to study the clot removal mechanism for the current mechanical thrombectomy devices (the suction catheter and the stent retriever) to understand the potential risks and propose device modifications and guidelines for clinical usage.

(2) The CA in this study is not aged while the clots in stoke patient are usually developed for hours or even days. The development of the clot microstructure can be studied by the scanning electron microscopy or computed tomography and related to the change of the mechanical properties. A new material model that is time variant can be built and more realistic CAs can be made.

(3) A computational model that couples the SPG clot cutting and the flow field by fluid-structure interaction can provide a better understanding of the clot chip evacuation process.

(4) The SPG modelling can be used to optimize the cutting tool geometry for clot cutting with smaller forces.

(5) The proposed SPG cutting simulation can be used in other machining processes with various kinds of cutting tool and workpiece.

(6) A cutting tool geometry that can induce cavitation at low rotational speed (< 10,000 rpm) can be investigated using the experimental setup and the CFD model.

(7) The clot cutting device development will be continued to achieve safe and complete clot remove all kinds of clots in any blood vessels or cavities besides the cerebral arteries. The experiment setup and CAs will be used for clinical study on animal and human cadaver in preparation for the first in human trial.